

Evolution of faint galaxy clustering:

The 2-point angular correlation function of 20,000 galaxies to $V < 23.5$ and $I < 22.5$.^{*}

Rémi A. Cabanac^{1**}, Valérie de Lapparent¹, and Paul Hickson²

¹ Institut d'Astrophysique de Paris, CNRS, 98 bis bvd Arago, 75014 Paris

² Dept. of Physics & Astronomy, UBC, 2219 Main Mall, Vancouver, BC V6T1Z4, Canada

Received ... /Accepted ...

Abstract. The UH8K wide field camera of the CFHT was used to image 0.68 deg^2 of sky. From these images, $\sim 20,000$ galaxies were detected to completeness magnitudes $V < 23.5$ and $I < 22.5$. The angular correlation function of these galaxies is well represented by the parameterization $\omega(\theta) = A_W \theta^{-\delta}$. The slope $\delta \simeq -0.8$ shows no significant variation over the range of magnitude. The amplitude A_W decreases with increasing magnitude in a way that is most compatible with a Λ CDM model ($\Omega_0 = 0.2, \Lambda = 0.8$) with a hierarchical clustering evolution parameter $\epsilon > 0$. We infer a best-fit spatial correlation length of $r_{00} \simeq 5.85 \pm 0.5 h^{-1} \text{ Mpc}$ at $z = 0$. The peak redshift of the survey ($I \leq 22.5$) is estimated to be $z_{peak} \sim 0.58$, using the blue-evolving luminosity function from the CFRS and the flat Λ cosmology, and $r_0(z_{peak}) \simeq 3.5 \pm 0.5 h^{-1} \text{ Mpc}$. We also detect a significant difference in clustering amplitude for the red and blue galaxies, quantitatively measured by correlation lengths of $r_{00} = 5.3 \pm 0.5 h^{-1} \text{ Mpc}$ and $r_{00} = 1.9 \pm 0.9 h^{-1} \text{ Mpc}$ respectively, at $z = 0$.

Key words: galaxies - angular correlation function - clustering - survey

1. Introduction

For the past decade, the study of the spatial Large-Scale Structure (LSS) of the universe has become an major tool for constraining the cosmological models. In particular, provided many assumptions on how morphological type correlates with colour, how mass is correlated with optical luminosity, and how local density correlates with morphology, recent CDM hierarchical N-body simulations and semi-analytic models of galaxy formation are able to make tentative predictions on the clustering evolution of the

galaxies as a function of their redshifts, spectral types and star formation rates (Kauffmann et al., 1999a; 1999b). By measuring redshifts for 10^5 or more galaxies, the next generation redshift surveys such as the VIRMOS survey (Le Fevre et al., 1998), the DEEP survey (Davis and Faber, 1998), and the LZT survey (Hickson et al., 1998; see also <http://www.astro.ubc.ca/LMT/lzt/index.html>) will allow detailed studies of the large-scale clustering and its evolution to $z \sim 1$.

Until these surveys are completed, the measurement of the 2-point angular correlation functions $\omega(\theta)$ of large photometric galaxy samples remains the best alternative to constrain galaxy clustering at $z > 1$. The major caveat of $\omega(\theta)$, as opposed to the 2-point spatial correlation function $\xi(r)$, is that it probes the projection of a 3D distribution of the galaxies onto the 2D celestial sphere. i.e. one can not tell whether a given galaxy is a faint nearby object or a bright remote one. As a consequence, $\omega(\theta)$ is sensitive to the effects of both the intrinsic 3D clustering and the luminosity evolution (LE) of galaxies for a given set of cosmological parameters. To avoid this degeneracy, one must choose between two approaches to extract sensible information from $\omega(\theta)$. First, one may use past observations to assume a scenario of galaxy evolution with given LEs and redshift distributions for each galaxy population, and then deduce the clustering evolution. A second approach would be to assume a clustering scenario, cosmological parameters, and to measure the evolution of the correlation function in order to validate the theoretical LE used to model the galaxy counts, e.g. Roche et al. (1993). In this paper, we favour the first approach. We use the Canada-France Redshift Survey (CFRS; Lilly et al. 1996) luminosity function and redshift distribution to invert the angular correlation function with Limber's formula (cf section 5 on modeling of $\omega[\theta]$, $\xi[r]$ and r_0) to compute the spatial correlation length from the amplitude of $\omega(\theta)$. This approach has several limits which are discussed in section 7.

An extensive literature covers the evolution of clustering using $\omega(\theta)$. The first attempts to describe clustering using counts in cells is due to Limber (1954). The two-

Send offprint requests to: cabanac@iap.fr

^{*} based on observations from the Canada-France- Hawaii Telescope

^{**} Fellow of Fonds FCAR, Québec

point correlation function as a statistical diagnosis of clustering has been popularized in astrophysics by Hauser & Peebles (1973) and applied to the Zwicky Catalog (Peebles and Hauser, 1974). Since these pioneering studies, the method, fully described by Peebles (1980), has been applied to many photographic catalogues in diverse photometric bands e.g. see Groth & Peebles (1977), Koo & Szalay (1984), Maddox et al. (1990b) where the clustering of local galaxies is studied on large angular scales. Using Limber's (1953) formula relating $\omega(\theta)$ to the spatial correlation function $\xi(r)$, these studies establish that the spatial clustering of local galaxies can be parameterized as a power law, $\xi(r) = (r/r_0)^{-\gamma}$, where the correlation length $r_0 \simeq 4 - 8h^{-1}$ Mpc ($h = H_0/100$) and the slope $\gamma \simeq 1.7 - 1.8$.

A second generation of studies based on small-scale CCDs, probes smaller areas to deeper magnitudes (Efsthathiou et al., 1991; Campos et al., 1995; Neuschaefer et al., 1992; Neuschaefer et al., 1995; Roukema and Peterson, 1994; Brainerd et al., 1995; Brainerd and Smail, 1998; Brainerd et al., 1999; Hudon and Lilly, 1996; Lidman and Peterson, 1996; Roche et al., 1993; Roche et al., 1996; Woods and Fahlman, 1997), therefore allowing to measure the evolution of the correlation length to redshifts $z \lesssim 1$). The most recent studies take advantage of large area CCD detectors (Roche and Eales, 1999; Postman et al., 1998) to measure the angular correlation function, and of the use of photometric redshifts (Koo, 1999) to estimate the spatial correlation function from deep photometric surveys (Villumsen et al., 1997; Arnouts et al., 1999). Despite these numerous studies, our knowledge of the clustering of galaxies is still rudimentary. The main trends are that while a mild luminosity evolution seems to be required to explain faint number counts in the I -band, weak or no evolution in the galaxy clustering with redshift is detected out to $z \sim 1$.

The existing surveys measuring the galaxy angular correlation function, and covering a broad range of magnitude bands and limits, constrain the value of $r_0(z_{peak})$ to the range $1.5 - 4.5 h^{-1}$ Mpc for $0.5 < z_{peak} < 1$. The dispersion is mainly due to the uncertainty in our knowledge of the luminosity functions and redshifts distributions for the different galaxy types at $z \sim 1$ (section 7), and possibly to the varying selection biases from survey to survey. To be consistent with the values of r_{00} measured from the nearby redshift surveys and ranging from $4h^{-1}$ Mpc to $8h^{-1}$ Mpc (de Lapparent et al., 1988; Loveday et al., 1992; Cole et al., 1994; Tucker et al., 1997; Ratcliffe et al., 1998; Guzzo et al., 1998), most observations of the galaxy clustering favour either constant or increasing clustering with time in proper coordinates, which is consistent with N-body simulations of CDM hierarchical universes (Davis et al., 1985; Baugh et al., 1999; Hudon and Lilly, 1996).

Note that only a few redshift surveys allow a direct study of the evolution of the spatial clustering (Lilly et al., 1995; Connolly et al., 1998; Arnouts et al., 1999;

Carlberg et al., 2000): these survey measure $r_0(z_{peak}) \simeq 1.4 - 4.5 h^{-1}$ Mpc for $0.5 < z_{peak} < 1$. We underline that except for the results of Carlberg et al. (2000), corresponding to the high value of $r_0(z_{peak})$, the limited area of the mentioned surveys make them very sensitive to cosmic variance, and the corresponding results on the correlation function must be taken with caution.

Moreover, the existing analyses have not yet answered convincingly to the following two questions: Is there an evolution of the angular correlation function slope $\delta = \gamma - 1$ at faint limiting magnitudes? And do red-selected objects and blue-selected objects show a true difference in 3-D clustering? In addition to providing another measure of the galaxy clustering at $z \simeq 0.5$, the new sample presented here allows us to address these questions. The paper is organized as follows, the observations are described in section 2, section 3 presents the data reduction, section 4 addresses the star/galaxy separations and counts. Section 5 details the analysis of the correlation function, section 6 gives the results, and section 7 provides a discussion of our results and a comparison with previous work.

2. Observations

The data were obtained during the spring of 1998 using the prime-focus wide-field UH8K CCD Camera (Metzger et al., 1995) at the Canada-France-Hawaii 3.6 m Telescope. The camera is a mosaic of 8 2k×4k CCD chips covering a total area of $\sim 28' \times 28'$ with a scale of $0.206''/\text{pixel}$. We observed four fields with R.A. offset of 23', 23', and 17', hence overlapping by 5', 5' and 10' (Table 1). The observations were done in bands V (Johnson) and I (Cousins). The total area of the survey is 0.68 deg^2 . The limiting magnitudes are $V < 24$ and $I < 23$ (see section 3.3 on the completeness). The central galactic coordinates are $l = 126.2^\circ$, $b = 68.2^\circ$. At such high galactic latitudes, the reddening is $E(B - V) < 0.03 \text{ mag}$ (Burstein and Heiles, 1982). This is an upper limit because we observed in V and I (reddening $\sim \lambda^{-1}$). We neglected both the absolute reddening and the relative reddening between the fields. Table 1 gives the characteristics of each field. The seeing is between $0.7''$ and $0.8''$ for both filters during the whole night. The exposure time is 1200 sec for all fields. Figure 1 shows the map of the $\sim 19,500$ galaxies detected to $I < 22.5$ (limiting magnitude of the correlation analysis, cf section 3.3). In spite of the bad cosmetics of CCD#4 (visible in the upper right corner of Fig. 1), the 5' overlaps provide homogeneous sampling of the area, except for the regions containing bright stars (empty circle in the upper middle) and the gaps within the UH8K Mosaic CCD chips.

3. Data reduction

The data were reduced using FLIPS by J.C. Cuillandre as part of the calibration service of the 1998 season of UH8K

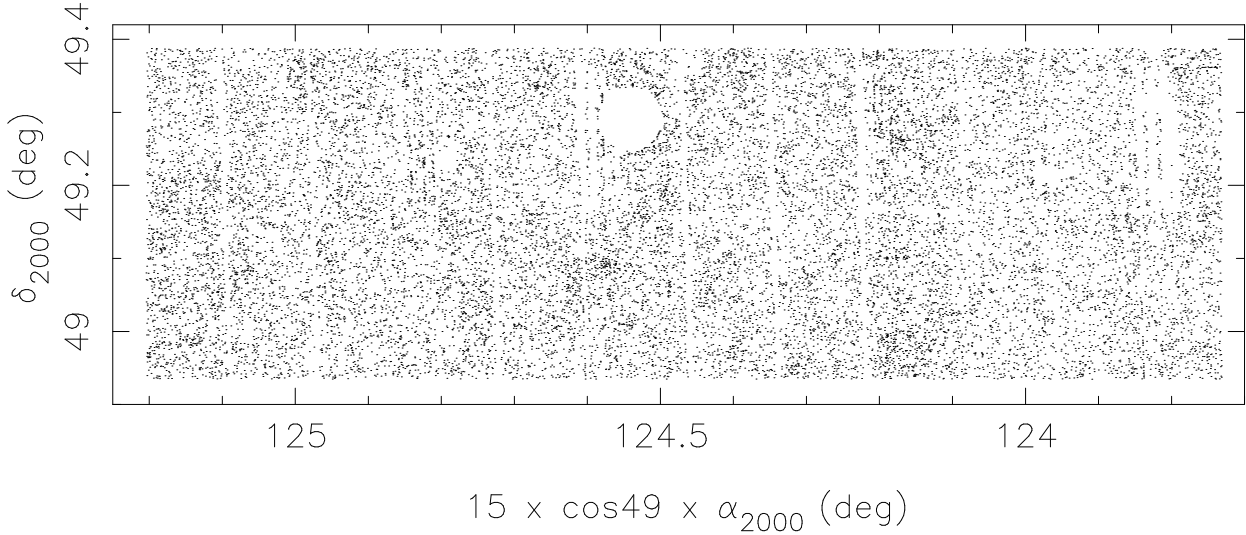


Fig. 1. Map of 19,506 galaxies to $I < 22.5$. Bad cosmetics, intervals between CCD chips, and saturation artifacts due to bright stars are masked (shown as empty areas).

Table 1. Field characteristics

Field	α_{2000} hr min sec	δ_{2000} ° ' "	airmass in V	airmass in I
UD02	12 37 55.3	+49 08 50.6	1.491	1.161
UD03	12 40 15.6	+49 08 52.3	1.371	1.148
UD04	12 42 35.8	+49 08 54.1	1.285	1.154
UD05	12 44 06.3	+49 08 55.3	1.224	1.176

Camera, Cuillandre (1998a; 1998b). FLIPS suppresses the dark and bias using the CCD overs-cans and flattens the response of the 8 detectors using a flat-field made by combining ~ 300 images of 18 nights of observation with the UH8K Camera. The final images have a corrected sky flux showing variations of less than 1% within each CCD image. The photometric standards were pre-reduced following exactly the same steps. The final dataset consists of 64 $2k \times 4k$ frames (32 in V , 32 in I), and a set of photometric standard stars.

Photometry was performed using the SExtractor Package (Bertin and Arnouts, 1996) which provides Kron-like elliptical aperture and isophotal fluxes, (X, Y) coordinates, position, elongation and stellarity class for all objects above a given threshold (we choose a threshold of 25 contiguous pixels above 1.5σ of sky value in V and I). The resulting SExtractor files were then calibrated for astrometry and photometry.

3.1. astrometry

The USNO-A2.0 Astrometric Catalogue (Monet, 1998) is used as the astrometric reference as it gives the equatorial

coordinates of most objects in our fields to a red mag < 20 with accuracies of $\leq 0.5''$, and because it is easily accessible via on-line astronomical databases. The astrometry is done separately on the 64 frames, with IRAF geomap/geotran second-order Legendre polynomials. A radial correction is applied previously on the (X, Y) coordinates to correct the prime-focus optical corrector distortion, whose equations were provided by J.C. Cuillandre (1996). If R is the actual radial coordinate of an object from the center of the UH8K mosaic (in mm) and r its observed radial coordinate (in mm), then the shift $r - R$ due to the corrector is

$$r - R = 9.07 \times 10^{-7} r^3 + 2.06 \times 10^{-12} r^5$$

$$r = 0.07284 \theta (1 + 2.593 \times 10^{-9} \theta^{2.093}). \quad (1)$$

θ is the angular distance of the object from the center in arcsec. According to eq. (1), the radial distortion is 0.13 pixel at a radius of $3'$, 0.32 pixel at $4'$, and it becomes non-negligible for radii greater than $6'$ where the distortion is greater than one pixel (e.g. the radial distortion at $14'$ is 14.1 pixels). The overlaps between the fields allow us to verify the importance of the optical distortion correction on the accuracy of the final astrometry. Figures 2 and 3 show the errors $\Delta\alpha$ and $\Delta\delta$ in X and Y directions for the overlap between the fields UD03 (CCD #0) and UD04 (CCD #6) without correction of distortion (Fig. 2) and with correction (Fig. 3). One can see that both the systematic errors and the random errors are below $0.5''$ after correction. We are not able to remove completely the systematic shifts between the fields (Fig. 3 frame a and b). This may be due to unknown misalignments between the chips of the mosaic. One can only minimize the system-

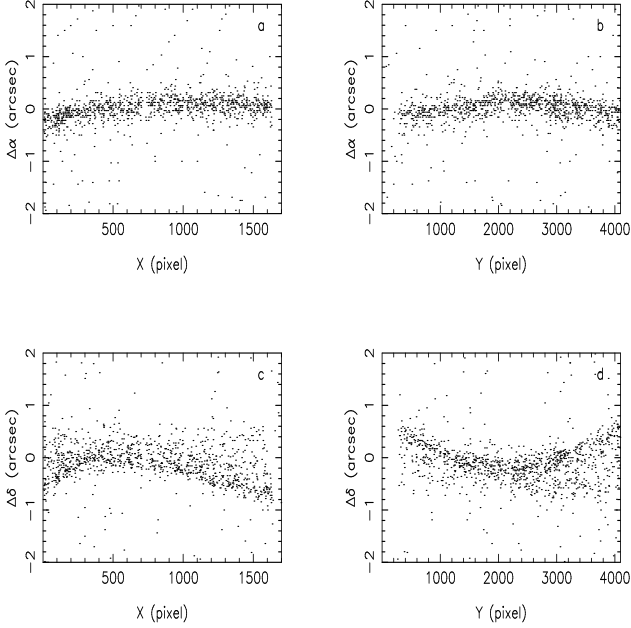


Fig. 2. Differences between the equatorial coordinates of the objects of the overlapping region of the fields UD03-CCD#0 and UD04-CCD#6 (in arcsec) if no correction is applied for the prime focus optical corrector distortion. (a) shows the right ascension difference $\Delta\alpha$ vs the CCD X axis, (b) shows $\Delta\alpha$ vs the CCD Y axis, (c) shows the declination difference $\Delta\delta$ vs the CCD X axis, and (d) shows $\Delta\delta$ vs the CCD Y axis. Important systematic effects are seen in frame (c) and (d).

atic effects to sub-arcsecond values. The final equatorial coordinates are precessed to J2000.

McCracken (priv. comm. 2000) used a finer and more complex approach with the Canada-France Deep Field (CFDF) ($\sim 1 \text{ deg}^2$ covering the CFRS in UBVRI, the fields in BVRI bands were observed with the UH8K Camera) by establishing an internal Word-Coordinate System to which all pointing are referred. The claimed dispersion is $0.3 \text{ pix} = 0.06''$ over the entire camera.

3.2. photometry

A rigorous photometric calibration is usually performed by applying a linear transformation on the instrumental

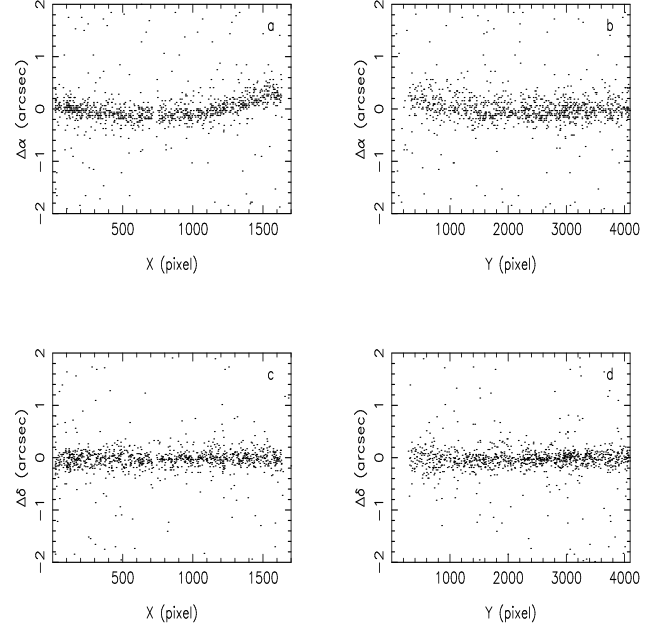


Fig. 3. Same as Fig. 2 with the correction of the prime focus optical corrector distortion of eq. (1).

(observed) magnitude m of the objects (given by SExtractor Kron-like elliptical aperture fluxes),

$$M = m - A_m \times \chi + k_m \times \Delta m + m_0, \quad (2)$$

where M is the standard magnitude, A_m is the extinction coefficient, χ is the airmass, k_m is the true-colour coefficient, Δm is the true colour and m_0 is the zero-point.

In principle, the coefficient A_m must be derived from the observation of a field of standard stars at three different airmasses, and the coefficients k_m , from a large range of star colours. Because the zero-points m_0 and the colour coefficients may vary from CCD chip to CCD chip, one should also observe the standard field separately in the 8 CCDs of the mosaic at least three times through the night.

For the UH8K Camera, this task is clearly beyond the observer's reach because the reading time of the UH8K camera is too long and the whole night would not be sufficient to observe the fields required for a proper photometric calibration. In fact, the dataset provided by the service observing consists of one field of standard stars SA104 (Landolt, 1992), observed in the middle of the night, in I and V . This minimal observation only allows one to measure an average zero-point over the whole mosaic in each

filter by combining all the standard stars (one or two per CCD chips).

We derive the colour coefficients k_V and k_I and the magnitude zero-points V_0 and I_0 by least-square fit of the colour transformation equations to the SA104 sequence:

$$(V - m_V) = k_V \times (V - I) + V_0 \quad (3)$$

$$(I - m_I) = k_I \times (V - I) + I_0 \quad (4)$$

The airmass correction is included in the m_V, m_I magnitudes, and we use the standard CFHT values for a thick CCD, $A_V = -0.12$ and $A_I = -0.05$ (<http://www.cfht.hawaii.edu/Instruments/Imaging/FOCAM/appen.html#F>) The results appear in Table 2. For comparison, the Table also lists another UH8K measurement obtained by J.C. Cuillandre as part of the calibration service of the UH8K 1996 season; no corresponding errors are provided.

For further control, we also derive the k_V and k_I coefficients from a synthetic standard sequence: synthetic “instrumental” magnitudes are computed for a set of stellar template spectra of different colours by a routine which uses the theoretical transmission curve of the instrument optics + filter (Arnouts, priv. comm. 1999). Application of eq. (3) and (4) to the synthetic sequence yields the “synthetic” k_V and k_I , also listed in Table 2. The corresponding zero-points V_0 and I_0 are derived in a second step by application of eq. (3) and (4) to all stars of the SA104 sequence, this time with the “synthetic” k_V and k_I .

The colour coefficient k_V derived from the synthetic sequence is compatible with the other values listed in Table 2. A significant dispersion appears in the k_I measurements, probably because this coefficient is small. The zero-points V_0 and I_0 listed in Table 2 are also consistent within the error bars and are poorly dependent on the colour coefficients. Because the colour coefficients k_V and k_I derived from SA104 display large errors, we choose to adopt the colour coefficients from the synthetic sequence and the corresponding zero-points calibrated on SA104: $k_V = -0.035 \pm 0.001$ and $k_I = 0.005 \pm 0.0003$; $V_0 = 24.58 \pm 0.018$ and $I_0 = 24.76 \pm 0.014$.

For all observed objects in the catalogue, the instrumental magnitudes are converted into standard V and I magnitudes by re-writing the colour equations eq. (3) and (4), written in terms of the standard colour $V - I$, into functions of the measured instrumental colours ($m_V - m_I$):

$$V = m_V - A_V \times \chi + \frac{k_V \times (m_V - m_I)}{1 + k_I - k_V} + V_0 \quad (5)$$

$$I = m_I - A_I \times \chi + \frac{k_I \times (m_V - m_I)}{1 + k_I - k_V} + I_0 \quad (6)$$

m_I, m_V are the observed magnitudes (Kron elliptical apertures), and k_V, k_I, V_0 and I_0 are the values labeled “synthetic” in Table 2. The other coefficients have the same

meaning as those of eq. (2), and we use, as in eq. (3) and (4), the standard CFH values $A_V = -0.12$ and $A_I = -0.05$.

The astronomer in charge of the service observing stated that the night was clear with only thin cirrus visible near the horizon at sunrise (Picat, priv. comm. 1998). The overlapping regions between the various mosaic fields observed can be used to estimate the possible variations in the zero-points during the night. The fields were observed in the following sequence: UD02-I, UD03-I, UD04-I, UD05-I, UD05-V, UD04-V, UD03-V, UD02-V. Figure 4 plots the average of the magnitude differences Δmag for the bright objects (with $I < 19$ and $V < 20$) detected in the overlapping CCD regions as a function of sidereal time. For each mosaic field observed, there are 2 to 4 CCD’s presenting an overlap with a CCD within another field, and each average Δmag is plotted at the sidereal time of the first observed overlap.

A small systematic variation of the average Δmag , denoted $\langle \Delta\text{mag} \rangle$, with sidereal time is detected in the I filter, and possibly in the V filter. A field-to-field correction of the zero-points is done to account for these small variations during the night: we apply to each field a correction in its zero-point measured by the $\langle \Delta\text{mag} \rangle$ in Fig. 4, taking the fields UD02-I and UD02-V as references, and following the sidereal sequence; the same zero-point correction is applied for all the CCD of each mosaic field. The residual magnitude variations measured after correction in the CCD overlaps are $\sigma \simeq 0.05$ mag in both the V and I filters. These put an upper limit on the variations in the zero-points and colour coefficients between the different CCD’s of the mosaic which are not accounted for in the present analysis. Note that a gradient remains in the V data (see section 6.3), which will be removed using the variation of the average galaxy number counts variations with right ascension.

To evaluate the final photometric errors in the obtained catalogue, the V and I magnitudes of objects in the overlapping sections are also compared individually. Figure 5 gives the residuals in the V and I bands versus magnitude for all objects having V-I colours (cf section 3.3) and Table 3 gives the corresponding standard deviations. The $V - I$ errors are taken to be $\sim \sqrt{2} \sigma_{\Delta V}$. The large dispersion at bright magnitudes in Fig. 5 is due to saturation effects. The “tilted” variation of the residuals with magnitude for residuals larger than 0.5 mag in absolute values (in both the V and I bands) is caused by the following effect: each object in the overlaps is given the magnitude measured in one of the overlap, arbitrarily. If the average of the 2 magnitudes in the overlap were used, this “tilt” would vanish. However, this affects only $\sim 0.5\%$ of the objects, and we consider that it would make no significant difference in any of the results reported here.

Table 2. Colour coefficients k for the V and I bands derived from the standard field SA104, J.C. Cuillandre’s calibration service, and S. Arnouts’ routine (labeled Synthetic, cf text). The average zero-points $\langle \text{zero-point} \rangle$ were derived using the associated k .

Source	Filter	k	$\langle \text{zero-point} \rangle$
SA104	V	0.0 ± 0.05	24.62 ± 0.06
SA104	I	0.041 ± 0.041	24.72 ± 0.05
Cuillandre	V	-0.033	24.629
Cuillandre	I	-0.066	24.721
Synthetic	V	-0.035 ± 0.001	24.58 ± 0.018
Synthetic	I	0.005 ± 0.0003	24.76 ± 0.014

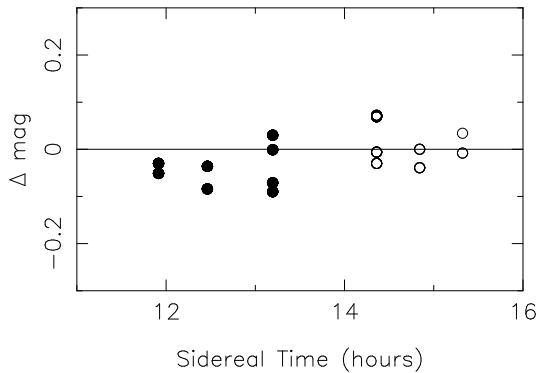


Fig. 4. Average magnitude differences Δmag of the bright objects present in the overlapping regions versus the sidereal time. The I -band data are shown as filled symbols, and the V -band data as open symbols. Time variations are always smaller than chip-to-chip zero-point errors.

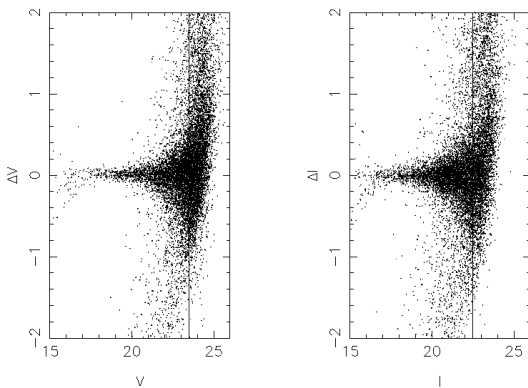


Fig. 5. Photometric residuals ΔV and ΔI in the overlapping frames versus magnitude V and I . The vertical lines indicate the completeness limits. The associated standard deviations are given in Table 3.

3.3. Magnitude and colour completeness

Three catalogues are generated from the data: one catalogue in the V band, one in the I band, and one catalogue containing objects with measured $V - I$ obtained by merging the two catalogues. All objects whose centroids

Table 3. Photometric errors in V and I (see Fig. 5). The errors combine random noise, residual variations from field-to-field in the zero-points during the night, and the uncorrected variations of the zero-points and colour coefficients from CCD-to-CCD within the mosaic.

V	N	$\sigma_{\Delta V}$	$\langle \Delta V \rangle$	I	N	$\sigma_{\Delta I}$	$\langle \Delta I \rangle$
15.5	2	0.018	0.029	15.0	3	0.030	-0.017
16.0	14	0.061	-0.021	15.5	23	0.046	0.037
16.5	14	0.076	-0.036	16.0	23	0.061	0.006
17.0	16	0.067	-0.002	16.5	37	0.016	0.023
17.5	27	0.048	-0.013	17.0	45	0.030	0.014
18.0	33	0.045	0.019	17.5	51	0.071	0.025
18.5	39	0.042	0.010	18.0	103	0.027	-0.005
19.0	69	0.048	0.002	18.5	108	0.047	0.011
19.5	106	0.060	-0.010	19.0	203	0.097	-0.029
20.0	138	0.105	-0.000	19.5	340	0.052	0.015
20.5	201	0.120	-0.011	20.0	498	0.122	0.043
21.0	321	0.143	-0.017	20.5	752	0.101	0.036
21.5	502	0.188	-0.030	21.0	1077	0.138	0.063
22.0	856	0.233	-0.039	21.5	1360	0.157	0.075
22.5	1244	0.274	-0.032	22.0	1666	0.238	0.072
23.0	2005	0.333	-0.049	22.5	1921	0.307	0.091
23.5	2596	0.379	-0.015	23.0	1712	0.407	0.120
24.0	2247	0.471	0.183	23.5	1003	0.505	0.138
24.5	887	0.574	0.398				

are separated by less than $1''$ were merged, and their $V - I$ are computed.

The completeness magnitudes of the V and I catalogues are defined to be one half magnitude brighter than the peak of the distributions. This corresponds to $V_{complete} \simeq 23.75$ and $I_{complete} \simeq 22.75$. Because some chips go deeper than others and because the correlation analysis is sensitive to chip-to-chip number density variations, we lower the completeness limit to the least sensitive chip (0.2 magnitude brighter), to which we add the chip-to-chip dispersion of $\sigma 0.05$ mag measured from Fig. 4. Hence, the final completeness limits are $V_{complete} \simeq 23.5$ and $I_{complete} \simeq 22.5$.

The colour completenesses in the V and I bands are given relative to one another in Fig. 6. The red galaxy completeness limit is determined primarily by how deep the V -band data extend. Because the V -band catalogue is only complete to $V \simeq 23.5$, faint objects redder than $V - I > 1$ will be missed near the limit of the I catalogue. (see Fig. 9 and 10 in section 4.3). This is an important fact to be remembered when making colour-selected correlation analyses.

4. Stars and galaxies

4.1. Star/galaxy separation

SExtractor computes a stellarity index for each detected object (in the interval 0-1, with 1 for stars, and 0 for galaxies). The stellarity index is determined from a non-linear set of equations (Trained Neural Network) (Bertin and Arnouts, 1996). The good seeing of the images ($0.7'' - 0.8''$) allows a robust classification to $V < 22$ and $I < 21$. According to Bertin & Arnouts, the algorithm success rate

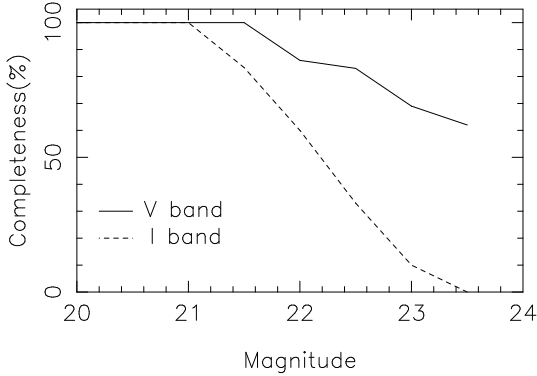


Fig. 6. Ratio of galaxies that are detected in the two bands (completeness) versus V and I magnitudes. At faint I magnitudes, the catalogue is biased against red objects

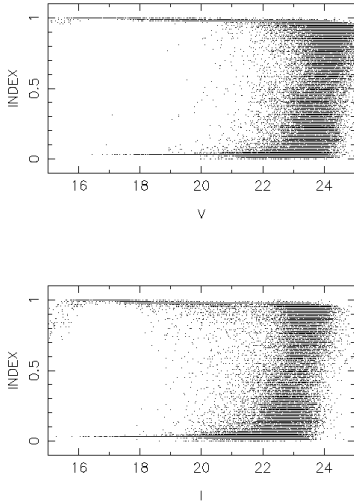


Fig. 7. SExtractor star/galaxy classification. Stars have value 1 and galaxies have value 0. The classification is robust up to $V < 22$ and $I < 21$

at these magnitudes is 95% using data with a similar sampling and a seeing $\sim 1''$. Figure 7 shows the index of the $\sim 30,000$ objects detected both in V and I . For $I < 21$ or $V < 22$, all objects with an index < 0.9 are classified as galaxies. This criterion classifies as galaxies only the objects showing a clear evidence of extendedness. For $I > 21$ or $V > 22$ objects with an index < 0.95 are classified as galaxies. Because at these faint magnitudes most objects have an index < 0.95 (the great majority of objects with a stellarity index higher than 0.95 are spurious detections), the threshold of 0.95 does not remove the remaining stars from the sample. To correct for the fact that most of the stars with $V > 22$ have been misclassified as galaxies, we need to apply a correction for the star dilution (see subsection on data-induced errors in section 5). We evaluated the stellar contamination with the Galaxy star-count model of Bahcall & Soneira (1986), which is compared on Figure 8 to the number counts of galaxies. The galaxies outnumber

the stars by nearly an order of magnitude where the classification algorithm efficiency is less than 95% (vertical dotted line in the lower part of the diagrams).

4.2. Galaxy counts

The galaxy counts shown in Fig. 8 are in good agreement with other measurements. In the I band, We systematically measure 20–30% more galaxies than Postman et al. (1998) up to $I < 22$. At $I = 21.25$, we count 5626 galaxies per deg^2 , and Postman et al. find 4057. Given the errors in the I zero-point calibration ($\sigma_{\Delta I} \sim 0.05 - 0.2$), the possible difference in the magnitude scale, and the intrinsic cosmic variance, we do not consider this difference to be significant.

We model the galaxy counts of Fig. 8 following the method described by Cole, Treyer, & Silk (1992). They give the equations of the volume element, the comoving distance and the luminosity distance of the objects for three cosmologies ($\Omega_0 = 1$, Einstein de Sitter; $\Omega_0 = 0.2$ Open; $\Omega_0 = 0.2$, $\Lambda = 3(1 - \Omega_0)H_0^2$ Flat, a factor c/H_0 is missing in their equation of the volume element for the flat Λ universe). Yoshii (1993) also details a similar method. The luminosity function (LF) is chosen to be similar to the CFRS for which LFs have been measured separately for blue and red galaxies (Lilly et al., 1995). Here we approximate the LF by its red component. The Schechter parameterization $\phi(M)$ is used (Schechter, 1976),

$$\phi(M)dM = 0.4 \ln 10 \phi^* 10^{X(1+\alpha)} dM \times \exp(-10^X),$$

$$X = 0.4(M^* - M), \quad (7)$$

where M is the absolute magnitude in the V or I band, and ϕ^* , M^* and α are the Schechter parameters (Here, $M_I^* = -21.5$, $\phi^* = 0.004$, $\alpha = -1.0$). K corrections are determined using 13-Gy-old elliptical galaxy template spectra from the PEGASE atlas (Fioc and Rocca-Volmerange, 1997), between redshifts $0 < z < 2$. As already noted by many authors, this simple model does not provide a satisfactory fit to the number counts at faint and bright magnitudes simultaneously for any cosmologies in the V -band. A better fit would include a more realistic luminosity function accounting for both the red and blue galaxy populations, and for either a density or a luminosity evolution (see section 6.1). As our purpose here is not to model the number counts, we limit ourselves to this partial model.

Figure 8 shows that our UH8K number counts deviate from the predicted counts in non-evolving Einstein-de Sitter and open universes at $I \gtrsim 21$ and at $V \gtrsim 22$. Postman et al. (1998) observed a clear departure from these two cosmological models in their I counts using the no-evolution model of Ferguson & Babul (1998) (FB). All other surveys displayed in both panels of Figure 8 (Arnouts et al., 1999; Cowie et al., 1988; Driver et al., 1994; Gardner et al., 1996; Postman et al., 1998; Woods and Fahlman, 1997; Mamon, 1998; McCracken et al., 2000a) have the same behaviour, except for the V number counts of Cowie et al.

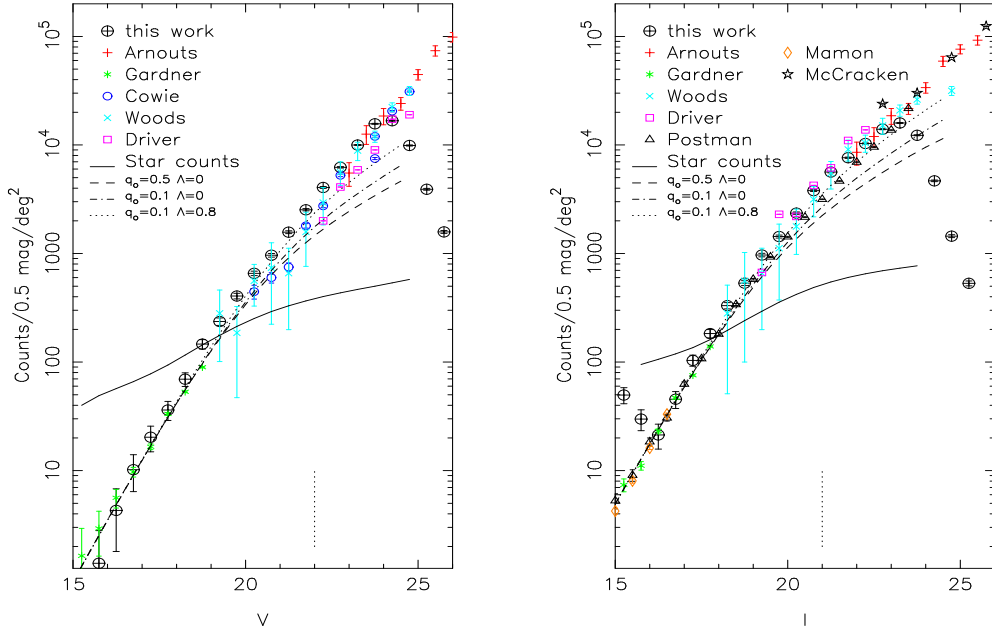


Fig. 8. Comparison of our UH8K galaxy counts in V and I with the results of Arnouts et al. (1999), Cowie et al. (1988), Drivers & Phillips (1994), Gardner et al. (1996), Postman et al. (1998), and Woods & Fahlman (1997), Mamon (1998), and McCracken et al. (2000a). Stars counts (solid line) are given according to the Bahcall model of the Galaxy. The vertical dotted line gives the limiting magnitude below which the star/galaxy classification is reliable (Fig. 7). Galaxy number counts are given for three cosmologies in V and I bands (cf text). The counts are in marginal agreement with a no-evolution flat Λ universe.

(1988), which agree well with the Einstein-de Sitter model at $V \leq 22$ and deviate only at fainter magnitudes.

In contrast, Figure 8 shows that the non-evolving flat Λ universe model provides a marginal agreement with our UH8K galaxy number counts in the I band at our magnitude limit of $I \simeq 22.5$. In fact, most surveys displayed in the right panel of Fig. 8 agree with this cosmological model at $I \lesssim 22$, as expected from the results of the CFRS (Lilly et al., 1996), where giant red galaxies evolve little in the redshift interval 0 – 1. In Fig. 8, the deviations from the non-evolving flat Λ universe occur in dataset which probe the faintest magnitudes, near $I \simeq 24$. Our sample is not deep enough to show a departure from this cosmological model. Lidman et al. also find that their I number counts (not shown in Fig. 8) are compatible with a no-evolution flat Λ universe (Lidman and Peterson, 1996) out to $I \simeq 21$, whereas they deviate from the evolution model of Yoshii (1993) (this model uses a dwarf galaxy blue LF, which yields very different K corrections at faint magnitudes compared to a no evolution model). From the mentioned surveys, there are indications that evolution should be used in the modeling of the I counts at $I > 22$, where significant departures from a non-evolving distribution occur.

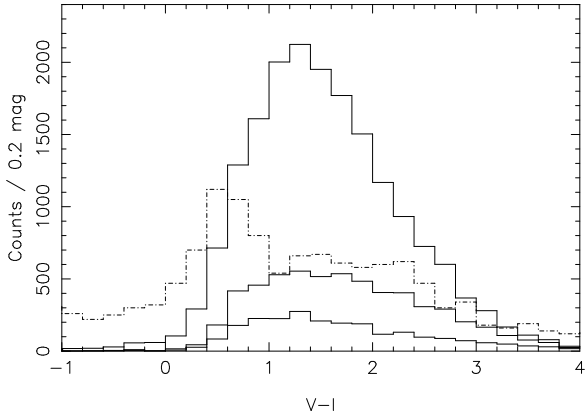
There is also marginal agreement of most V number counts displayed in the left panel of Fig. 8, including our UH8K data, with a non-evolving flat Λ universe model. The deviations from the model occur in a wider range of V magnitude, namely at $V \gtrsim 22 - 24$, depending on the data set, and the deviation is greater than for the I counts. This may be partly explained by the fact that the V number counts are more sensitive to evolution of the blue galaxy population than the I counts.

4.3. Galaxy colours

Figure 9 shows histograms of galaxies and stars versus $V - I$ colours. For galaxies, histograms are given for three limiting magnitudes, $I < 20$, $I < 21$, and $I < 22.5$. The corresponding median $V - I$ colours are 1.45, 1.57, and 1.38. Figure 10 shows $V - I$ colours vs I magnitudes for the sample of $\sim 30,000$ detected galaxies. A vertical line shows the I -band completion limit $I = 22.5$ and an oblique line shows $V - I$ colour limits accessible due the V -band completion limit of $V = 23.5$. There is no visible trend towards a strong colour evolution of the galaxies with their magnitudes, but a robust conclusion is not possible because the I sample is depleted in red objects. A natural

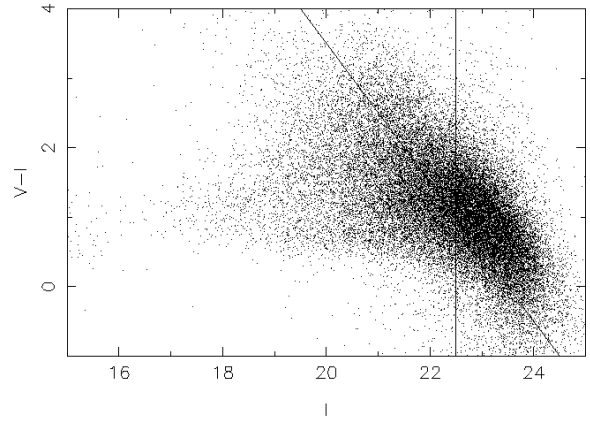
Table 4. Differential V and I -band galaxy counts (see Fig. 8).

V	N	σ_N	I	N	σ_N
15.75	1.4	1.4	15.75	29.8	6.5
16.25	4.3	2.5	16.25	21.3	5.5
16.75	10.2	3.8	16.75	45.4	8.0
17.25	20.3	5.4	17.25	103.6	12.1
17.75	36.2	7.2	17.75	183.1	16.1
18.25	69.6	10.0	18.25	330.8	21.7
18.75	146.4	14.6	18.75	533.9	27.5
19.25	236.3	18.5	19.25	968.4	37.1
19.75	406.0	24.3	19.75	1434.2	45.1
20.25	656.9	30.9	20.25	2355.7	57.8
20.75	964.2	37.4	20.75	3794.2	73.4
21.25	1571.8	47.7	21.25	5626.0	89.3
21.75	2531.7	60.6	21.75	7626.8	104.0
22.25	4058.5	76.7	22.25	10312.0	121.0
22.75	6219.1	95.0	22.75	13972.8	140.8
23.25	9991.9	120.4	23.25	15936.6	150.4
23.75	15665.8	150.7	23.75	12284.4	132.0
24.25	16725.8	155.7			
24.75	9894.8	119.8			

**Fig. 9.** Histogram of galaxy counts (solid line) from top to bottom $I < 22.5$, $I < 21$, $I < 20$ and star counts (dot-dashed line) vs $V - I$ colour. The star counts are scaled up by an order of magnitude. Only stars brighter than $I < 19$ are included.

although arbitrary value to divide red galaxies from blue galaxies is the median of the histogram with $I < 22.5$ in Fig. 9, located near $V - I = 1.4$. In the rest of the paper red galaxies will be those having $V - I > 1.4$ and blue galaxies will be those having $V - I \leq 1.4$.

5. Analysis

**Fig. 10.** Galaxy $V - I$ colours vs I magnitude. The vertical line indicates the completeness limit $I = 22.5$. The oblique line shows the $V - I$ colours accessible at the completeness limit $V = 23.5$.

5.1. Estimation of $\omega(\theta)$

The 2-point angular correlation function $\omega(\theta)$ is calculated by generating samples of random points covering the same area and having the same number as the galaxy sample. We use the estimator $W(\theta)$ defined by Landy & Szalay (1993) (hereafter LS), which has the advantage of reduced edge effects and smallest possible variance:

$$W(\theta) \equiv W = \frac{DD - 2DR + RR}{RR}, \quad (8)$$

where DD is the number of galaxy-galaxy pairs, DR the number of galaxy-random pairs, and RR is the number of random-random pairs, all of a given angular separation θ . Following Roche (1996; 1999), we set a logarithmic binning for the separation defined as $\Delta \log(\theta) = 0.2$. The numerical approach of LS is used to calculate DD , DR and RR . If one defines the variables d and x as

$$d = \frac{DD}{G_p(\theta)n(n-1)/2}, \quad (9)$$

$$x = \frac{DR}{G_p(\theta)n^2}, \quad (10)$$

$$G_p(\theta) = \langle RR \rangle / [n(n-1)/2], \quad (11)$$

then eq. (8) can be re-written as

$$W = d - 2x + 1. \quad (12)$$

$G_p(\theta)$ is the probability of finding two randomly placed galaxies separated by a distance $\theta \pm d\theta/2$, n is the number of real galaxies in the sample, and $\langle RR \rangle$ is the average over N realizations of a random sample of k points, with $Nk = 100,000$ (k varies between 10 to 100 depending on the magnitude interval in which the angular correlation

function is measured). LS also define $G_t(\theta)$, the probability of finding two neighbors both at a distance $\theta \pm d\theta/2$ of one given object.

$$G_t(\theta) = \langle n_t(\theta) \rangle / [n(n-1)(n-2)/2], \quad (13)$$

where $\langle n_t(\theta) \rangle$ is the average number of unique triplets. $G_t(\theta)$ is necessary to evaluate the random errors (cf section 5.3).

5.2. Modeling of $\omega(\theta)$, $\xi(r)$ and r_0

The canonical parameterizations of the two-point spatial correlation function $\xi(r)$ (Phillipps et al., 1978) and of the angular correlation function $\omega(\theta)$ (Peebles, 1980) are

$$\xi(r, z) = \frac{(r/r_{00})^{-\gamma}}{(1+z)^{3+\epsilon}} \quad \text{and} \quad \omega(\theta) = A_\omega \theta^{-\delta} \quad (14)$$

where r is the comoving distance, r_{00} the correlation length at $z = 0$, θ the angular separation in radian, A_ω is the amplitude of angular correlation function, γ and δ are the slopes ($\delta = \gamma - 1$) and ϵ is a parameter characterizing the evolution of clustering with the redshift z . If $\epsilon > 0$ the clustering evolves in proper coordinates, if $\epsilon = 0$ the clustering is constant in proper coordinates hence increases in an expanding universe, if $\epsilon = -1.2$ the clustering is constant in comoving coordinates. The comoving correlation length at a redshift z is related to r_{00} by

$$r_0(z) = r_{00}(1+z)^{-(3+\epsilon-\gamma)/\gamma}. \quad (15)$$

Given eq. (14) and the galaxy redshift distribution $N(z)$, one can relate $\omega(\theta)$ and $\xi(r)$:

$$\omega(\theta) = C r_0(z_{peak})^\gamma \theta^{1-\gamma} B(\epsilon), \quad (16)$$

$$B(\epsilon) = \left(\frac{c}{H_0}\right)^{\gamma-1} \int_0^\infty \frac{r_d(z)^{1-\gamma} N(z)^2}{g(z) (1+z)^{3+\epsilon}} dz \times \left[\int_0^\infty N(z) dz \right]^{-2}, \quad (17)$$

$$N(z) = (\pi/180)^{-2} \int_{m_1}^{m_2} \sum_i \phi_i(M, z) \frac{dV}{d\omega}, \quad (18)$$

$$g(z) = \left[(1+z)^2 \sqrt{1 + \Omega_0 z} \right]^{-1} \quad (\Lambda = 0), \quad (19)$$

$$g(z) = \frac{(1+z)^{-1}}{\sqrt{\Omega_0(1+z)^3 - \Omega_0 + 1}} \quad (\Lambda + \Omega_0 = 1), \quad (20)$$

$$C = \sqrt{\pi} \frac{\Gamma[(\gamma-1)/2]}{\Gamma(\gamma/2)} \simeq 3.68 \quad . \quad (21)$$

Here $r_d(z)$ is the angular diameter distance, $dV/d\omega dz$ is the comoving volume element, both given for three cosmologies in the appendix of Cole, Treyer and Silk (1992). $\sum_i \phi_i(M, z)$ is the luminosity function, whose definition might be dependent on different spectral type i evolving with z , and Γ is the gamma function. The value of C is given for a typical value of $\gamma = 1.8$ (Peebles, 1980). Equations (16) to (21) allow to make a direct derivation of

$r_0(z_{peak})$ from $A_\omega(\Delta m)$, where z_{peak} is the peak of the redshift distribution of the galaxies in the sample defined by the interval of apparent magnitude Δm :

$$r_0(z_{peak}) = \left[\frac{A_\omega(z_{peak})}{C B(\epsilon)} \right]^{1/\gamma}. \quad (22)$$

($A_\omega(\Delta m)$ is rewritten as $A_\omega(z_{peak})$).

5.3. Estimation of errors

In the past few years, considerable theoretical efforts have been devoted to the calculation of errors in the estimation of $\omega(\theta)$. The errors can be divided into two categories; (1) the random errors; and (2) the systematic errors due to the various observational biases in the data. The systematic errors are caused by false detections, star/galaxy misidentifications, photometric variations and astrometric errors. The random errors are induced by the finite area of the survey and depend on the geometry and the size of the sample.

5.3.1. Random errors

Until recently, a Gaussian approximation for the distribution of the galaxies was assumed to calculate the errors on $\omega(\theta)$. However, the distribution of the galaxies is known to depart significantly from a Gaussian distribution on small scales. A finer approach would be to include the possible correlations of the data into the error analysis. This has been done by Bernstein (1994) on the LS estimator $W(\theta)$. Bernstein derives a formal solution to the random errors for the case of a hierarchical clustering universe in the limits $n \gg 1$ (number of galaxies in the sample), $W \ll 1$, and $\theta \ll$ angular size of the sample:

$$\left(\frac{\Delta W}{W}\right)^2 = 4(1 - 2q_3 + q_4) \overline{W}_{\theta_{max}} + \frac{4}{n} \left[\frac{W_r(1 + 2q_3 W)}{W^2} + q_3 - 1 \right] + \frac{2}{n^2} \left[(G_p^{-1} - 1) \frac{1 + W}{W^2} - W^{-1} - 1 \right], \quad (23)$$

where the parameters q_3 and q_4 are measured by Gaztañaga (1994). They are related to the hierarchical amplitudes s_3 and s_4 ($s_n \equiv \langle \omega_n \rangle / [\langle \omega_2 \rangle]^{n-1}$, where ω_n are the n -point angular correlation functions), by $q_3 \simeq s_3/3$ and $q_4 \simeq s_4/16$ (Gaztañaga, 1994). s_3 and s_4 have been derived by Gaztañaga (1994) and Roche & Eales (1999) from the APM catalogue (Maddox et al., 1990a): $s_3 \simeq 4$ and $s_4 \simeq 50$ at $\theta \sim 0.1^\circ$, the scale at which the angular-correlation function is well measured in the APM catalogue (Maddox et al., 1990b); therefore $q_3 \simeq 1.3$ and $q_4 \simeq 3$. W_r (r for ring) is the 3-point angular correlation for triplets of galaxies defined by 2 galaxies at a distance in the interval $[\theta, \theta + \delta\theta]$ from the 3rd galaxy. In principle, W_r is marginally greater than $W(\theta)$ as defined

in eq. (8) but $W_r \simeq W$ is a fair approximation. $\overline{W}_{\theta_{max}}$ is the average value of the angular correlation function at the largest angular separation of the sample. This quantity is not directly accessible because the estimator W is biased by finite volume errors at separations similar to the size of the survey. To get an estimation of $\overline{W}_{\theta_{max}}$ we divide our sample into 8 sub-samples (one separation at mid-declination and three separations in right ascension) and measure the LS estimator W . Then, assuming a power-law whose slope is set at the small angles we extrapolate the value $W_{\theta_{max}}$ for each sub-sample. Finally, $\overline{W}_{\theta_{max}}$ is obtained as the average over the 8 sub-samples. Subdividing the sample into 8 sub-samples also allows to measure the error on W independently at all scales (the largest angular separation being a quarter of the largest full survey separation), by simply taking the variance over the 8 sub-samples. The resulting variance largely underestimates the variance defined in eq. (23).

5.3.2. Systematic errors

The cosmic bias or integral constraint: The measurement of $\overline{W}_{\theta_{max}}$ provides the cosmic bias b_W as

$$b_W(\theta) \simeq (3 - 4 q_3 - W(\theta)^{-1}) \overline{W}_{\theta_{max}}. \quad (24)$$

(Colombi, priv. comm. 1999). This bias can be corrected in the calculation of $W(\theta)$ in the form of an additive factor IC . At small angular separations eq. (24) simplifies as $b_W \simeq -\overline{W}_{\theta_{max}}/W$. This negative bias is very small but becomes comparable to W when θ approaches the angular size of the sample. The usual way of correcting for the cosmic bias is to fix a slope for the angular correlation function and to find the constant value of IC which minimizes the χ^2 fitting to the data. One may point out that the cosmic bias becomes non-negligible only when the errors $\Delta W/W$ of the LS estimator given by eq. (23) are large. The smallest scale at which b_W is $\gtrsim 10\%$ is $\theta \geq 3'$, which corresponds to the last 2 points in all curves plotted in Figures 12 and 13. In the interval $17 < I < 21$ for example, $b_W \simeq -0.09$. However, the random errors at this scale are also significant, $\Delta W/W \simeq 12\%$, which gives little weight to these points in the least-square fits of $W(\theta)$. We therefore consider that the cosmic bias has negligible impact on our reported slope and correlation amplitude, and we chose to ignore the cosmic bias in order to avoid introducing a prior information on the slope of $W(\theta)$.

Misidentified stars: Because stars are uncorrelated on the sky as shown on Fig. 11, the stars fainter than $V > 22$ and $I > 21$ which are not removed from the catalogue dilute the clustering present in the galaxy correlation, i.e. decrease the amplitude of $\omega(\theta)$. The usual way of correcting for this bias (Postman et al., 1998; Woods and Fahlman,

1997) is to apply a star dilution (multiplicative) factor D_{star} to the parameterized amplitude A_ω .

$$D_{star} = \left(\frac{N_{obj}}{N_{obj} - N_{star}} \right)^2, \quad (25)$$

where N_{obj} is the number of objects in the galaxy samples, and N_{star} is the number of stars predicted by the Bahcall model of the Galaxy (Bahcall, 1986). For $V < 22$ and $I < 21$, N_{star} is given by the classification efficiency of 95% of SExtractor, namely the upper value is 5% of the number of stars detected, so $D_{star} < 1.1$. The values of D_{star} for fainter limiting magnitudes are given in Table 5.

Masking: Although the SExtractor programme is very good at avoiding false detections, it is sometimes tricked by the diffraction patterns and large wings of bright stars as would be any code using an isophotal threshold for detection. Because such false detections are strongly clustered, they increase the correlation amplitude at scales corresponding to the angular size of the false structure. To prevent the systematic patterns which could be introduced by false detections, we define two masks, one covering the bad pixels, columns and regions, and one covering all stars brighter the $V < 15$ (from the HST Guide Star Catalog). The second mask is made of four empirical components, (1) a central disk whose radius is defined by an exponential law as a function of magnitude ($radius = 4969 \exp[-0.378 Mag]$ pixels), (2) a vertical rectangle covering the bleeding streak, whose length is an exponential function of magnitude ($bleed = 1.28 \times 10^7 \exp[-0.8 Mag]$ pixels), (3) and (4) inclined rectangles (at 38.5° and 51° of the vertical axis) covering the diffraction spikes, also following exponential law of the magnitude ($spike = 5292 \exp[-0.315 Mag]$ pixels). The masked regions are partially visible in Fig. 1 because only bright stars show large wings and the low density of objects does not permit one to distinguish "true" empty regions from masked regions. We apply the same two masks to the random realizations for the evaluation of LS estimator $W(\theta)$ in section 5.1.

Photometric errors: Two kinds of photometric errors may be present: the random errors or photon noise called σ_M , and the residual calibration errors in the coefficients A_V , A_I , k_V , k_I and the zero-points V_0 and I_0 . Note that the errors given in Table 3 called $\sigma_{\Delta V}$ and $\sigma_{\Delta I}$ include both the random and calibration errors. It is difficult but necessary to evaluate quantitatively the two kinds of errors because they have opposite qualitative effects on the angular correlation function.

The random errors can be evaluated from Table 3. It is clear that at bright magnitudes, the calibration errors dominate while random errors dominate at faint magnitudes. A random error in a galaxy apparent magnitude is equivalent to an increase of the possible volume in which

that galaxy lies, i.e. it is equivalent to a convolution of the de-projected distance interval. Hence, the random error erases the clustering present in the sample. It is difficult to evaluate directly the decrease in the amplitude of $\omega(\theta)$ due to the random errors because it is impossible to disentangle it from a real variation of the spatial galaxy clustering. Nevertheless, one can follow a simple argument to estimate how random errors affect the measurement of $\omega(\theta)$. First, assume that the galaxy number counts follow a power-law $\log N = \alpha \text{ mag} + \text{cst}$ so the relative error is $\Delta N/N = (\alpha/\log e)\Delta \text{mag}$. An extreme case is to consider that all the galaxies with a magnitude error superior to the magnitude bin for which $\omega(\theta)$ is evaluated (~ 0.5), are uncorrelated to the sample actually falling in the bin. This is an extreme case because many of the galaxies with the large error in magnitude do belong to the bin. In that case, these galaxies would have a very similar effect on the amplitude of $\omega(\theta)$ as if they were stars. So the multiplicative diluting factor D_{gal} of the random photometric error would be,

$$D_{gal} = (1 - (\alpha/\log e)\Delta \text{mag})^{-2}, \quad (26)$$

where Δmag is the magnitude error and α is the slope of the galaxy number count power-law. Taking the best fit slope $\alpha \simeq 0.4$ (see Fig. 8 and Table 4), a typical magnitude error of 0.15 (see Table 3) leads to a dilution factor of $D_{gal} \simeq 1.3$, of order of the star dilution factor D_{star} given in Table 5. This estimate of D_{gal} is an indicative upper limit, and cannot be used to correct for the dilution due to random errors in the magnitude of the galaxies because the prior condition is that these galaxies are uncorrelated. This assumption might not be true, and the correction would then artificially increase the amplitude of the correlation function.

We now evaluate the calibration error budget. Because the largest airmass difference in V is 0.267, and 0.028 in I , even a 50% error on A_V and A_I would not produce more than $\Delta V \sim 0.015$ and $\Delta I \sim 7 \times 10^{-4}$. If we assume that the chip-to-chip error on k_V is given by the difference between the values of the synthetic sequence and the measurement of Cuillandre in Table 2 (this is certainly not the case for k_I , because Cuillandre's value is too low) then in the most extreme colours $(V - I) \sim 4$ (only a very small fraction of our sample), the resulting magnitude difference would be $\Delta V \sim 0.008$. The case of k_I is not clear, although it seems reasonable to assume that the error cannot be more than ten times the error ΔV , so $\Delta I < 0.08$. The residual systematic errors in the zero-points have been evaluated in section 3.2 to be $\sigma \simeq 0.05$. Combining all these mentioned sources of calibration errors, one finds a value of 0.053 in V and an upper value of 0.094 in I .

The residual photometric errors have an opposite effect on $W(\theta)$. Namely, they introduces CCD-to-CCD variations in the galaxy number counts wrongly interpreted by the correlation analysis as intrinsic clustering on a scale

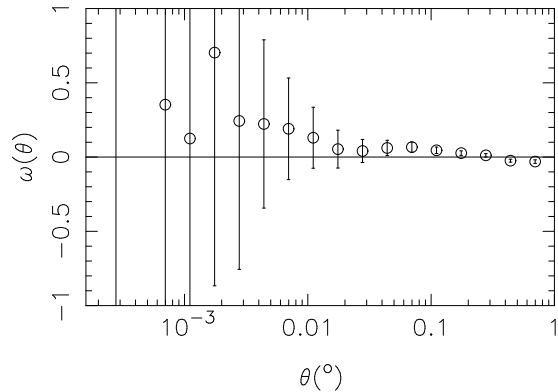


Fig. 11. Angular correlation function of stars brighter than $I < 21$. The error bars show 1σ Poisson noise. The result is compatible with a random distribution.

given by the angular size of the individual CCD chips, thus artificially increasing the amplitude of $\omega(\theta)$ on these scales. Geller, de Lapparent & Kurtz (1984) showed that plate-to-plate systematic variations of more than 0.05 mag introduced in the Shane-Wirtanen catalogue would produce a flattening of the correlation function and an artificial break at a scale corresponding to the plate size. For that reason, we limit our measurement of the angular correlation to $\theta \lesssim 400'' \simeq 0.1^\circ$, corresponding to the smallest dimension of the individual CCD's. We point out that the combined effect of random and zero-point errors would be to flatten artificially the slope of $\omega(\theta)$, as Geller et al. demonstrated.

Astrometric errors: Small scale astrometric errors are likely to become significant when the bin size of $\omega(\theta)$ is of the order of the error. The trivial method to avoid such contamination is to limit the analysis to bins greater than the errors, i.e. greater than $0.5''$ in our case. When one builds a mosaic survey combining overlapping patches of the sky, systematic astrometric errors may come into play: the number of objects may be artificially higher or smaller in overlapping regions just because of misidentifications. This would induce a similar effect on the amplitude of correlation to the zero-point errors at an angular scales of the order of the field size. However, a comparative analysis of the number counts of overlapping regions with other parts of the field does not show any significant bias toward a higher number of objects in the overlapping regions. We therefore consider that our astrometric errors have a negligible effect on $\omega(\theta)$, and we limit its calculation to $\theta > 1''$.

Table 5. Star dilution correction factor D_{star} in V and I bands

V	D_{star}	I	D_{star}
22.25	1.08	21.25	1.23
22.75	1.11	21.75	1.20
23.25	1.10	22.25	1.17
23.75	1.09	22.75	1.15
24.25	1.08	23.25	1.13

6. Results

First, we tested the reliability of our code for measuring the LS estimator of $\omega(\theta)$ on the Zwicky catalogue. The result is consistent with that of Peebles (1974). We also used a deep catalogue (courtesy of Roukema, priv. comm. 1999) and found good agreement with its $\omega(\theta)$ measurement.

Figure 11 shows the result of our angular correlation code on the sample of stars brighter than $I < 21$. We limit the calculation of $W(\theta)$ at 0.1° because of the reasons invoked in section 5. The function is always consistent with a random distribution. The weak positive signal might be a sign of misclassification of galaxies or simply small overdensities. The LS estimator (eq. [12]) is then measured, using the entire sample of galaxies, for six cumulative magnitude intervals: $17 < I < 20$, $17 < I < 20.5$, $17 < I < 21$, $17 < I < 21.5$, $17 < I < 22$, and $17 < I < 22.5$, and four incremental magnitude intervals: $20 < I < 21$, $21 < I < 21.5$, $21.5 < I < 22$, and $22 < I < 22.5$.

Random errors are computed using eq. (23). Table 6 gives the values of $W(\theta)$ and the $3\text{-}\sigma$ random errors for each cumulative magnitude interval, while Table 7 gives the best-fitted values of the corresponding $W(\theta)$ for the parameterization of eq. (14). Three values of the amplitude are given in Table 7. A_W is the best-fit amplitude when both the slope and the amplitude are fitted. $A_W^{0.8}$ is the best-fitted amplitude when the slope is constrained to $\delta = 0.8$, and A_W^{star} is $A_W^{0.8}$ corrected for the star dilution factor ($I > 21$) $A_W^{star} = A_W^{0.8} \times D_{star}$. The amplitudes A_W , $A_W^{0.8}$, and A_W^{star} correspond to the values of the correlation function at 1° , the usual chosen reference scale. Table 7 shows the results for both the integrated intervals and incremental intervals of magnitudes. All quoted errors are $3\text{-}\sigma$. For the same I_{median} , the values of $A_W^{0.8}$ are consistent between the integrated intervals and the incremental intervals. Because the error bars are larger for the incremental intervals, we based our analysis on the integrated intervals only. Figure 12 plots the LS $W(\theta)$ in logarithmic scale for the I -band incremental magnitude intervals, along with the best-fit power-laws for an unconstrained slope (Table 7). Figure 13 plots the difference of all $W(\theta)$ with the constrained $\delta = 0.8$ power-laws.

A final check on the code was done by Colombi (priv. comm. 1999) using a count-in-cells routine. The results showed that the quality of the dataset allows to measure

higher orders of the distribution of galaxies (skewness & kurtosis). The measurements of the angular correlation in the interval $17 < I < 21$ gave consistent results with the LS estimator.

Here, we only show the correlation function in the I band. We also measured $W(\theta)$ on the V -band map in the magnitude intervals $17 < V < 21.5$, $17 < V < 22$, $17 < V < 22.5$, $17 < V < 23$, and $17 < V < 23.5$. The values of the amplitude A_W obtained in the V band are very similar to the values obtained in I , but the average slope δ is $\simeq 0.5 - 0.6$ in V , as compared to $\simeq 0.8 - 0.9$ in I . Neuschaefer & Windhorst (1995) also measured slopes $\delta \simeq 0.5$ in the g and r bands and $\delta \simeq 0.7 - 0.8$ in the i band.

6.1. Variation of slope versus magnitude

Recent Λ CDM models predict a decrease of the spatial correlation slope γ for scales $< 10h^{-1}$ Mpc from $\gamma = 1.8$ at $z = 0$ to $\gamma \simeq 1.6$ for $z \geq 1$ (Kauffmann et al., 1999). This implies a decrease of the slope $\delta = \gamma - 1$ of $W(\theta)$ at small angular scales and faint magnitudes. Observational evidences are poorly conclusive. Brainerd et al. (1999) report a steepening of the slope on small scales while Campos et al., 1995, Neuschaefer and Windhorst, 1995, Infante and Pritchet, 1995, and Postman et al. 1998 find the opposite effect. Other authors find no significant variations to the limits of their samples (Couch et al., 1993; Roche and Eales, 1999; Hudon and Lilly, 1996; Woods and Fahlman, 1997). Figure 13 and Table 7 show no significant flattening of slope at faint magnitudes. The slope is compatible with $\delta = 0.8$ for all magnitude intervals. Our result is nevertheless consistent with the results of Postman et al. (1998) who find signs of a decrease only in their faintest bins, at $I > 22$, near and beyond our I limit.

6.2. Variation of A_W with magnitude

The choice of a galaxy luminosity function to model the decrease of A_W with the limiting apparent magnitude is crucial because the behavior of A_W is sensitive to both the parameterized characteristic absolute magnitude M^* and the slope α (eq. [7]). We choose to use the luminosity function observed in the CFRS (Lilly et al. 1996), derived from 591 galaxies in the range $0 < z < 1$, keeping in mind that such a small sample of galaxies can only provide an indication of a general trend. Because both the CFRS sample and our sample have been selected in the I band, we thus limit the possible biases due to the photometric sample selection.

Lilly et al. divide the CFRS sample into a red population (redder than an Sbc having rest-frame $[U - V]_{AB} = 1.38$; $[U - V]_{AB} \simeq [V - I]_{AB}$ at $z \sim 0.5$, $V_{AB} = V$, and $I_{AB} = I + 0.48$) and a blue population (bluer than an Sbc). The red galaxies show no density or luminosity evolution in the range $0 < z < 1$, whereas the blue galaxies

Table 6. Measures of $W(\theta)$ and $3\text{-}\sigma$ errors (from eq. [23]) in the I band for $17 < I < 20$ (W_{20}), $17 < I < 20.5$ ($W_{20.5}$), $17 < I < 21$ (W_{21}), $17 < I < 21.5$ ($W_{21.5}$), $17 < I < 22$ (W_{22}), and $17 < I < 22.5$ ($W_{22.5}$).

θ arcsec	W_{20}	$3\sigma_{20}$	$W_{20.5}$	$3\sigma_{20.5}$	W_{21}	$3\sigma_{21}$	$W_{21.5}$	$3\sigma_{21.5}$	W_{22}	$3\sigma_{22}$	$W_{22.5}$	$3\sigma_{22.5}$
	($\times 10^{-3}$)											
1.0	-753	538	-750	359	-1068	242	-545	210	-469	150	-377	110
1.6	538	1041	-134	429	136	299	-84.0	176	-61.1	119	-222	83.3
2.5	1467	889	1346	574	760	309	554	194	422	124	291	78.6
4.0	430	389	650	301	570	204	380	123	334	86.8	311	66.9
6.3	767	356	561	216	446	143	392	105	287	66.6	226	46.3
10.0	464	212	359	134	291	90.8	236	63.3	180	41.6	146	29.8
15.8	372	152	272	95.0	267	75.5	182	46.6	136	30.3	121	23.5
25.1	331	123	215	69.7	171	48.3	122	31.1	95.3	20.9	86.5	16.6
39.8	209	77.9	160	50.3	127	35.1	94.2	23.5	71.3	15.4	63.4	12.2
63.1	145	54.1	112	35.3	71.6	20.7	56.4	14.5	45.3	10.1	41.2	8.06
100.0	83.5	32.4	70.1	22.7	49.7	14.6	35.3	9.41	30.2	6.89	27.5	5.54
158.5	55.8	22.2	43.8	14.9	26.4	8.45	21.5	6.10	17.8	4.36	17.2	3.65
251.2	30.5	13.4	22.0	8.50	13.3	4.95	10.3	3.43	10.7	2.86	7.09	18.2
398.1	16.4	8.38	3.19	2.99	2.30	1.93	-1.23	0.51	1.61	0.95	1.09	6.37
631.0	-2.29	-1.40	-4.12	1.15	-2.27	0.68	-1.80	0.56	-0.48	0.11	-1.44	0.40
1000.0	-7.00	-2.18	-5.14	1.62	-2.47	0.96	-0.50	0.16	-0.64	0.31	1.17	0.56
1584.9	-3.04	1.88	-1.85	1.84	-4.98	1.26	-5.00	0.93	-3.68	0.73	-2.50	0.53
2511.9	-32	7.91	-1.58	2.35	-9.85	0.86	2.27	1.21	1.15	0.33	-2.56	0.54

Table 7. Best-fit values of the amplitude A_W and the slope δ of $W(\theta) = A_W\theta^{-\delta}$; $A_W^{0.8}$ is obtained for a fixed slope $\delta = 0.8$ and A_W^{star} is the corresponding star dilution corrected amplitude (see text) in the interval $10'' < \theta < 500''$. All quoted errors are 3σ . The first 6 rows of the table show the integrated intervals of magnitudes, the last 4 rows show the incremental intervals of magnitudes.

I Magnitude		N_{gal}	A_W $\times 10^{-4}$	δ	$A_W^{0.8}$ $\times 10^{-4}$	A_W^{star} $\times 10^{-4}$
Interval	Median					
17-20.0	19.356	2166	40.4 ± 61.3	0.839 ± 0.329	47.9 ± 19.6	47.9
17-20.5	19.807	3552	31.7 ± 40.8	0.830 ± 0.277	36.1 ± 12.5	36.1
17-21.0	20.281	5671	15.6 ± 17.8	0.917 ± 0.240	25.8 ± 8.02	25.8
17-21.5	20.724	8739	11.42 ± 11.87	0.930 ± 0.218	19.95 ± 5.48	19.95
17-22.0	21.166	13215	12.6 ± 11.4	0.861 ± 0.190	16.6 ± 3.85	19.4
17-22.5	21.617	19501	10.06 ± 7.80	0.872 ± 0.161	13.8 ± 2.88	15.9
20-21.0	20.610	3504	9.35 ± 14.4	0.981 ± 0.320	20.0 ± 8.12	20.0
21-21.5	21.270	3068	6.67 ± 14.9	0.947 ± 0.477	12.36 ± 7.05	15.2
21.5-22	21.772	4476	10.3 ± 17.6	0.880 ± 0.372	14.5 ± 5.82	17.5
22-22.5	22.267	6283	11.2 ± 14.0	0.810 ± 0.277	11.7 ± 4.01	13.7

show a luminosity evolution of about 1 magnitude in the same redshift range. Recent measurements made from the CNOC2 survey (Lin et al., 1999), on ~ 2000 galaxies in the range $0.1 < z < 0.7$, confirms the general observations of the CFRS, although the proposed interpretation is notably different. The CNOC2 analysis separates the luminosity evolution from the density evolution. Early and intermediate (red) galaxies show a small luminosity evolution in the range $0.1 < z < 0.7$ ($\Delta M^* \simeq 0.5$), whereas late (blue) galaxies show a clear density evolution with almost no luminosity evolution in the same redshift range, in apparent contradiction with the CFRS results.

We choose to adapt the CFRS LF to our sample, and we proceed as follows. Galaxies are separated into two

broad spectro-photometric groups, the E/S0/Sab (called red) and the Sbc/Scd/Irr (called blue), using the median colour $V - I = 1.4$ (see section 4.3). The red group has a non-evolving luminosity function with parameters $\phi^* = 0.0148 h^3 \text{ Mpc}^{-3}$, $M_I^* = -21.5 + 5 \log 10h$, and $\alpha = -0.5$ (eq. [7]), and the blue group has a mild-evolving luminosity function with parameters $\phi^* = 0.015 h^3 \text{ Mpc}^{-3}$, $M_I^* = -21.56 + (1 - e^{-2z}) + 5 \log 10h$, and $\alpha = -1.07$. The factor $1 - e^{-2z}$ equals 0 for $z = 0$ and ~ 1 for $z \geq 1$ and mimics the observed smooth brightening of M_I^* with redshift.

We integrate eq. (18) in the different apparent magnitude intervals listed in Table 6, and obtain $N(z)$ for three cosmologies. The K corrections are computed from tem-

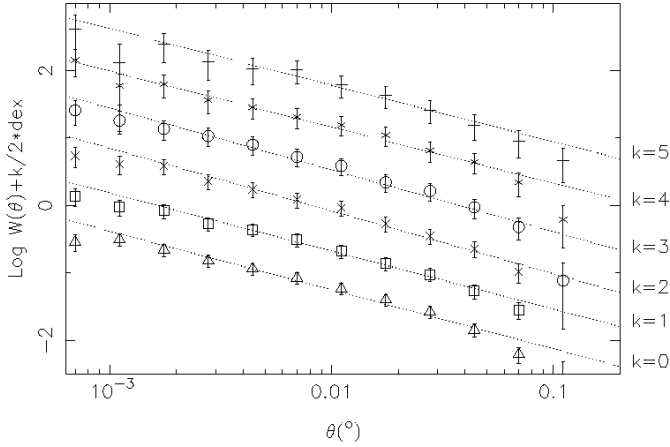


Fig. 12. Plots of $\text{Log } W(\theta)$ spaced by 0.5 dex (symbols; see also Table 6) and best-fit curves (A_W and δ of Table 7) as dotted line. From top to bottom, $17 < I < 20$ ($k=5$), $17 < I < 20.5$ ($k=4$), $17 < I < 21$ ($k=3$), $17 < I < 21.5$ ($k=2$), $17 < I < 22$ ($k=1$), $17 < I < 22.5$ ($k=0$)

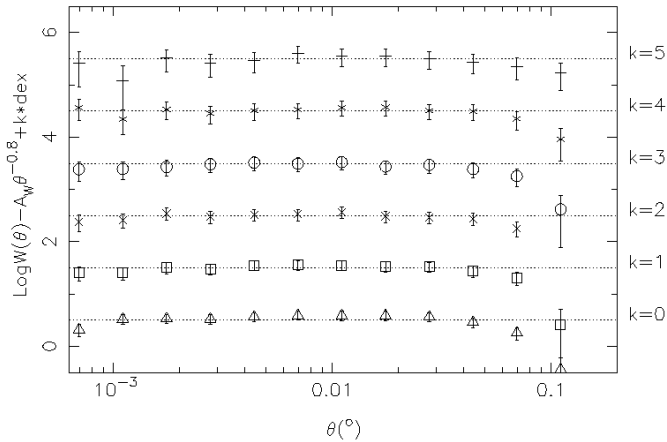


Fig. 13. Plots of the differences of the LS $W(\theta)$ and the best-fit $A_W^{0.8}\theta^{-0.8}$ (dotted lines). The curves are spaced by 1 dex for sake of clarity. Same magnitude intervals as Fig. 12.

plates of E (9 Gy) for the red group and Sd (13 Gyr) for the blue group from the PEGASE atlas (Fioc and Rocca-Volmerange, 1997) and are shown in Fig. 14. The choice of a given atlas is not benign, as Galaz (1998) shows that K corrections can vary by 50% at $z \sim 1$ when comparing the PEGASE atlas with the GISSSEL atlas (Bruzual and Charlot, 1993), leading to significant differences in $N(z)$.

Figure 15 shows $N(z)$ for red and blue objects having $I < 22.5$, for three cosmologies: Einstein-de Sitter $\Omega_0 = 1$

as a solid line, open universe $\Omega_0 = 0.2$ as a dashed line, and flat Λ $\Omega_0 = 0.2$ universe as a dotted line. One can note that red and blue galaxies show very different redshift distributions as expected from the different LFs. This should be kept in mind when we compare the different evolution of A_W with magnitude for the red and blue samples. The resulting $N(z)$ used to model our sample is the sum of the $N(z)$ for the red and blue object distributions respectively. As our 2 colour samples suffer from differential incompleteness (see section 3.3), we normalized the relative number of blue and red objects to the observed ratio in the CFRS survey at the corresponding limiting magnitude.

Figures 16, 17, and 18 show the decrease of the amplitude of the correlation function corrected for star dilution A_W^{star} for the median I magnitude of the integrated and incremental intervals (Table 7); a fixed slope of $\delta = 0.8$ is used to measure the reference scale, which is taken a 1 degree. The data-points for the incremental intervals show larger error bars, but are consistent with the amplitudes for the integrated intervals. The measurements of Postman et al. (1998) and Lidman & Peterson (1996) are shown for comparison. We also plot the expected curves for the three universes mentioned above, for each of the three values of the clustering parameter $\epsilon = -1.2$ in Fig. 16, $\epsilon = 0$ in Fig. 17, and $\epsilon = 0.8$ in Fig. 18). For each value of ϵ , the theoretical curves are calculated with $\delta = -0.8$ and the best-fit spatial correlation length r_{00} at $z = 0$, using eq. (15) and (22). These values along with the corresponding χ^2 of the fit are listed in Table 8 (only the integrated intervals of magnitude are used for the fitting, 6 data-points). Note that in Fig. 16, 17, and 18, different values of r_{00} shift the theoretical curves by constant values in the Y direction.

Several conclusions can be drawn from Fig. 16, 17, 18, and Table 8. We can always find a set Ω_0 , ϵ and r_0 which fits our data. Λ universes with $\Omega_m = 0.2$ and $\Lambda = 0.8$ slightly favour null ϵ , in good agreement with the results of Baugh et al. (1999) for semi-analytical models of biased galaxy formation. In contrast, Table 8 shows that Einstein-de Sitter universes favour positive ϵ (recall that $\epsilon = -1.2$ means no evolution in comoving coordinates, and $\epsilon = 0$ no evolution in physical coordinates), as obtained by Hudon & Lilly (1996) ($\epsilon = 0.8$) for the hierarchical clustering CDM model of Davis et al. (1985) in Einstein-de Sitter Universes. Third, positive values of evolution parameter ϵ give better fits to our observations (Fig. 18) than negative ϵ . Moreover, comparison of the r_{00} listed in Table 8 with the local values of $r_{00} \simeq 4 - 8h^{-1}$ Mpc at $z \simeq 0$ also suggest null to mild clustering evolution.

Finally, Table 9 gives the peak redshift z_{peak} derived from the redshift distributions $N(z)$ (using the CFRS model luminosity function) for all magnitude intervals and for the three cosmologies. Using eq. (22), the values of $r_0(z_{peak})$ are computed for all z_{peak} , and can be compared to other results. At $z \simeq 0.5$, we measure a value of $r_0(z_{peak})$ in the range $3.4 - 3.7h^{-1}$ Mpc, depending on the cosmological model and the evolution index ϵ . The

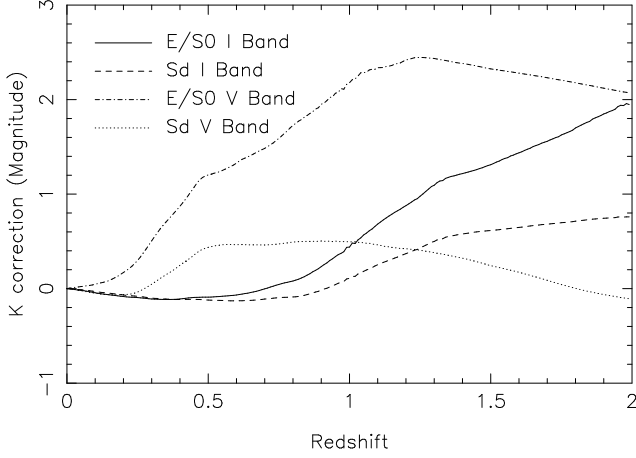


Fig. 14. K corrections for early-type and late-type galaxies in V & I band. We use the simplest hypothesis of non-evolving galaxy spectra over the range $0 < z < 2$.

typical $1\text{-}\sigma$ uncertainty on the values of $r_0(z_{peak})$ listed in Table 9 is $\sim 0.35 h^{-1}$ Mpc. The additional error originating from the uncertainty in the cosmology and in ϵ is estimated from Tables 8 and 9 to be $\sim 0.35 h^{-1}$ Mpc. By adding these errors in quadrature, we find an estimated total error in the correlation length r_0 of $\sim 0.5 h^{-1}$ Mpc. This more realistic error can also be applied to the values of r_0 given in Table 8.

If we assume a flat $\Lambda = 0.8$ cosmology, Table 9 gives $r_0(z_{peak}) \simeq 3.5 \pm 0.5 h^{-1}$ Mpc at the peak redshift $z_{peak} \sim 0.58$ of the $I \leq 22.5$ survey. The corresponding value at $z_{peak} \sim 0.50$ is $r_0(z_{peak}) \simeq 3.7 \pm 0.5 h^{-1}$ Mpc. Within the error bar, this result is in agreement with most other angular correlation measurements at $z_{peak} \simeq 0.5$ (Postman et al., 1998; Hudon and Lilly, 1996; Roche and Eales, 1999; Woods and Fahlman, 1997).

If we compare with the direct spatial measurements, our result is closer to the CNOC2 results than those from the CFRS: Carlberg et al. find that the 2300 bright galaxies in the CNOC2 survey (Yee et al., 1996) show little clustering evolution in the range $0.03 < z < 0.65$ with $r_0 \simeq 3.5 - 4.5 h^{-1}$ Mpc at $z \sim 0.5$, depending on the cosmological parameters (Carlberg et al., 2000); whereas Le Fèvre et al. measure $r_0 \simeq 1.5 h^{-1}$ Mpc at $z \sim 0.5$ for 591 I-selected galaxies, implying a strong evolution from the local values ($r_0 \simeq 4 - 8 h^{-1}$ Mpc at $z \simeq 0$) (Lilly et al., 1995). As mentioned above, the small correlation length found in the CFRS survey may be due to the cosmic variance which affects small area surveys. On the other hand, neither the CNOC2 survey nor the CFRS survey detect an evolution in the slope $\gamma \sim 1.8$, in good agreement with our UH8K data.

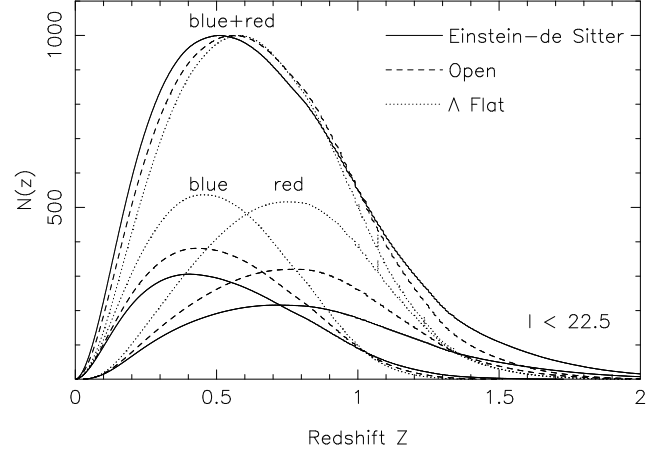


Fig. 15. Redshift distributions $N(z)$ for red and blue objects assuming CFRS-like LF. The limiting magnitude is $I < 22.5$. The peaks of the red+blue distributions are normalized to 1000. The relative number of blue and red objects are normalized to the observed ratio in the CFRS survey.

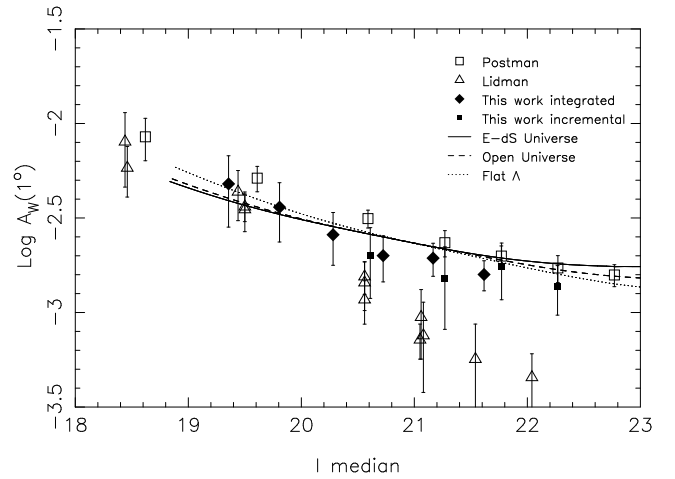


Fig. 16. The amplitude of correlation A_W^{star} for the UH8K data is plotted against the median I magnitude for the same intervals as in Fig. 12 and 13 (filled symbols) and is compared to the results from other groups. The four filled squares with large error bars are the measurements for the incremental intervals, and the diamonds show the values for the integrated intervals (see also Table 7). Theoretical curves are calculated for $\epsilon = -1.2$ and the corresponding best-fit r_0 (listed in Table 8) obtained with $\delta = -0.8$, and for three universes: Einstein-de Sitter as solid lines, $\Omega_0 = 0.2, \Lambda = 0$ as dashed lines and $\Omega_0 = 0.2, \Lambda$ flat universe as dot-dashed lines. We use the bimodal CFRS luminosity function with mild luminosity evolution described in subsection 6.2.

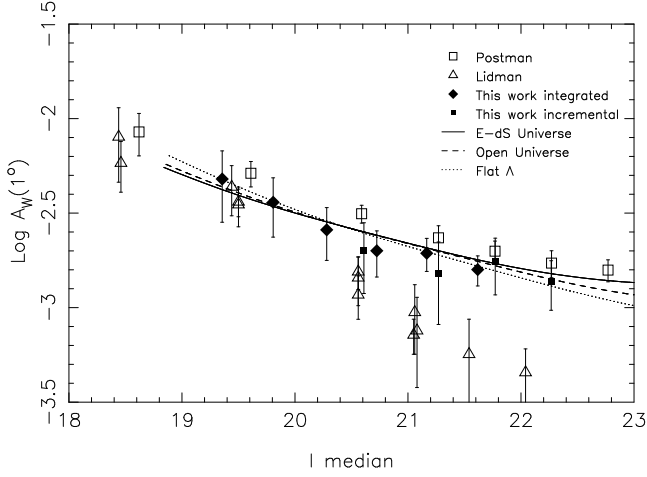


Fig. 17. Same as Fig. 16, but with $\epsilon = 0$ for the theoretical curves. The corresponding best-fit r_{00} are given in Table 8.

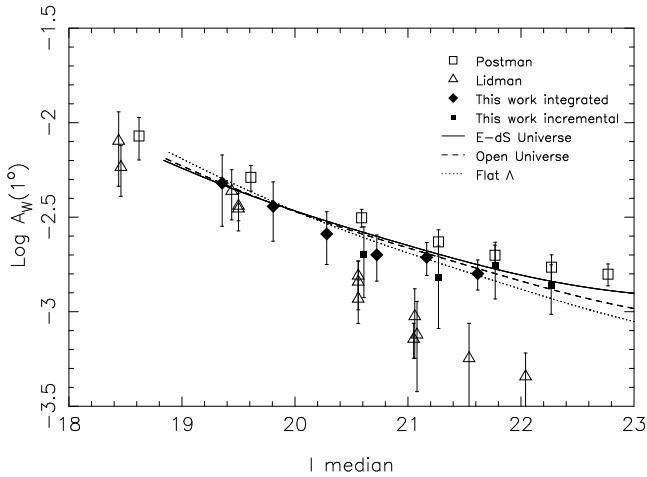


Fig. 18. Same as Fig. 16, but with $\epsilon = 0.8$ for the theoretical curves. The corresponding best-fit r_{00} are given in Table 8.

Table 8. Best-fit values of the spatial correlation length r_{00} for fixed ϵ and three cosmologies.

r_{00} h^{-1} Mpc	ϵ	Cosmology		χ^2
		Ω_0	Λ	
3.53 ± 0.28	-1.2	1	0	0.0115
3.49 ± 0.41	-1.2	0.2	0	0.0125
4.11 ± 0.21	-1.2	0.2	0.8	0.00676
4.43 ± 0.33	0	1	0	0.00499
4.38 ± 0.28	0	0.2	0	0.00367
5.03 ± 0.28	0	0.2	0.8	0.00232
5.31 ± 0.31	0.8	1	0	0.00269
5.19 ± 0.34	0.8	0.2	0	0.00218
5.85 ± 0.35	0.8	0.2	0.8	0.00233

Table 9. Redshift z_{peak} of the peak of the redshift distribution $N(z)$ and the corresponding best-fit correlation lengths $r_0(z_{peak})$ for different magnitude intervals and cosmologies. Here $\epsilon = 0.8$

I Magnitude		z_{peak}	r_0	z_{peak}	r_0	z_{peak}	r_0
Interval	Median	E.-de S.	Open	Flat	Flat	Λ	Λ
17-20.0	19.356	0.295	3.98	0.295	3.89	0.295	4.39
17-20.5	19.807	0.325	3.88	0.325	3.80	0.330	4.26
17-21.0	20.281	0.355	3.78	0.365	3.67	0.385	4.07
17-21.5	20.724	0.400	3.65	0.420	3.52	0.440	3.90
17-22.0	21.166	0.455	3.50	0.485	3.34	0.510	3.70
17-22.5	21.617	0.505	3.37	0.565	3.16	0.575	3.53

6.3. Variation of A_W with galaxy colour

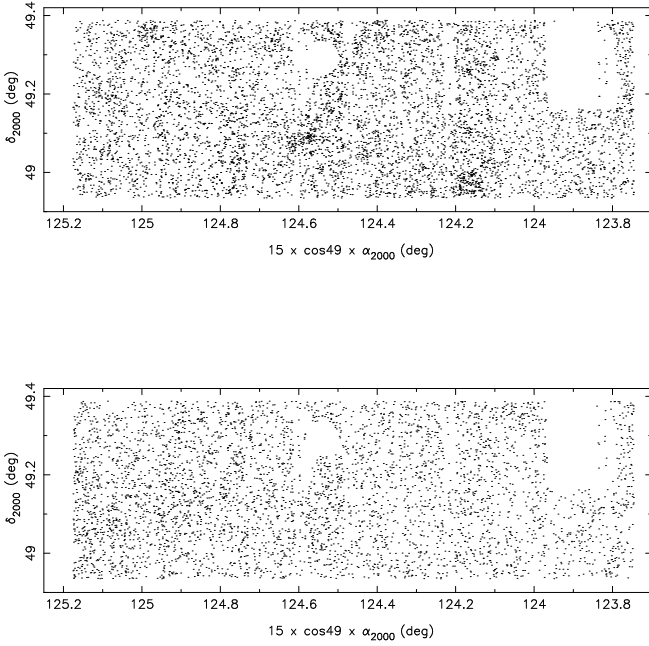
We also calculate the variations of A_W with depth for the blue and red sub-samples of our UH8K data, which are defined in subsection 4.3. A map of the 8986 red galaxies ($V - I > 1.4$) with $I \leq 22$ is shown in Figure 19 (top panel); the 7259 blue galaxies ($V - I < 1.4$) to the same limiting magnitude are plotted in the bottom panel of Figure 19. One can see that red objects are more clustered than blue objects, as partly reflected by the morphology density relationship (Dressler, 1980). Note that the surface density of the blue galaxies increases by a factor of ~ 2 with increasing right ascension. This is probably caused by a systematic drift in the photometric zero-point along the survey R.A. direction, which was not completely removed by the matching of the magnitudes in the CCD overlaps (see subsection 3.2). We then perform an angular correlation analysis on each colour-selected sample. For the blue sample, we introduce in the random simulations, prior to masking, the mean R.A. gradient measured from the data.

Figure 20 shows the decrease of A_W for the red and blue galaxies to a limiting magnitude $I < 22.5$ (see section 3.3 & 4.3). In principle, the separation should be done on rest-frame colours and not on observed colours, but this requires prior knowledge of the redshift of the objects. The effect of using observed colours is to decrease the resulting angular correlation because galaxies of different intrinsic colours at different distances are mixed together. We use the same angular binning as in the previous analyses for consistency (subsections 6.1 & 6.2). Table 10 gives the median magnitude of the red and blue samples. The last interval given in Table 10 includes all 11,483 red galaxies ($I_{med} = 21.670$) and 20,743 blue galaxies ($I_{med} = 22.902$) fainter than $I > 17$ (to $V \simeq 24$ and $I \simeq 23$).

Note that the blue sample reaches fainter I magnitudes than the red sample. As seen in the section 3.3, this is a selection effect due to the fact that only galaxies detected in the 2 bands are shown in the sample, and the blue sample is complete to $V \sim 24$. Thus at $I = 22.5$, the galaxies redder than $V - I > 1.5$ (in fact most of the red sample) show sparse sampling. Each interval in Table 10 is respectively complete for galaxies having $V - I < 3, 2.5, 2, 1.5$. We emphasize that the last two intervals of the red sam-

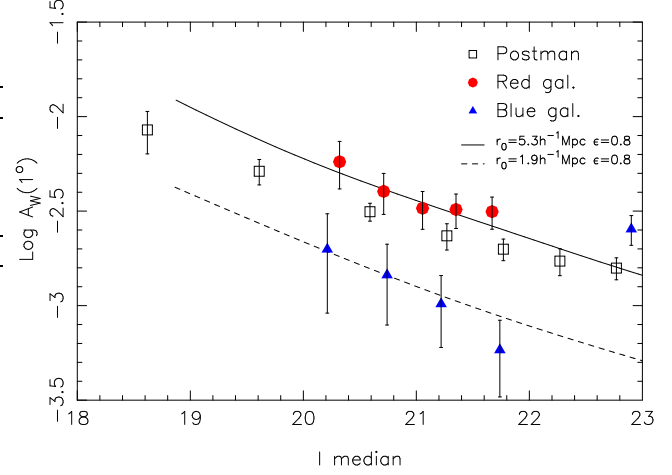
Table 10. Median magnitude I_{median} of the red and blue samples for the different cumulative I magnitude intervals.

Mag. interval	# red gal.	I_{median}^{red}	# blue gal.	I_{median}^{blue}
17-21	3379	20.212	1854	20.212
17-21.5	5057	20.711	2934	20.741
17-22	7069	21.055	4589	21.219
17-22.5	8986	21.351	7259	21.739
>17	11483	21.670	20743	22.902

**Fig. 19.** Map of 7069 red galaxies with observed $V - I > 1.4$ (top) and 4589 blue galaxies with observed $V - I < 1.4$ (bottom) to $I < 22$.

ple ($17 < I < 22$ and $17 < I < 22.5$) are probably too incomplete to be considered as fair samples. The incompleteness induces two competing effect. On the one hand, it increases A_W , because the number of objects is artificially small and the resulting correlation is higher; on the other hand, it makes the median magnitude brighter (cf Table 10), thus inducing a steepening of the slope of the A_W decrease. In Fig. 20, the obviously erroneous offset of last point for the blue sample, corresponding to the full magnitude range $I > 17$ and a median I magnitude of ~ 22.9 , also illustrates the error on the measurements of A_W one can expect in extreme cases where magnitudes are poorly defined and objects are under-sampled.

Keeping in mind the warning of the previous paragraphs, and the fact that the error bars prevent us from drawing strong conclusions, it is striking to see the differ-

**Fig. 20.** Same as Fig. 16. The galaxies of our sample are divided into red galaxies with $V - I > 1.4$ (filled octagons) and blue galaxies with $V - I \leq 1.4$ (filled triangles). The results for the full sample of Postman et al. (1998) (open squares) are shown for reference. Best-fit models are shown for a Λ flat universe with $\epsilon = 0.8$ for red galaxies using CFRS red LF (solid line) and blue galaxies using CFRS blue LF with mild evolution (dashed line).

ent amplitude of A_W for the two colour samples shown in Fig. 20. The larger A_W for red galaxies than for blue galaxies for all I_{median} is in agreement with the well-known higher clustering amplitude of early-type galaxies (see for recent spatial measurements in the Stromlo-APM survey by Loveday et al., 1995), which is partly reflected by the morphology density relationship (Dressler, 1980). Using the first three data-points of the red sample and blue samples in Fig. 20, we calculate that the two distributions are different at a $4\text{-}\sigma$ level. The corresponding clustering amplitudes are $r_0(z_{peak}) = 5.3 \pm 0.5 h^{-1}$ Mpc for the red sample and $r_0(z_{peak}) = 1.9 \pm 0.9 h^{-1}$ Mpc for the blue sample; both are based on a Λ universe with $\epsilon = 0.8$. For the purpose of comparing these values of $r_0(z_{peak})$, the mentioned errors assume that the correlation functions for the red and blue galaxies have the same slope $\delta \simeq 0.8$. This may not be true (see Loveday et al. 1995), but our UH8K sample does not allow to address this issue. We also ignore the systematic effect of the cosmology which would affect the values of $r_0(z_{peak})$ for the two populations in the same direction. The resulting difference in the measured $r_0(z_{peak})$ for the red and blue populations are at the $3\text{-}\sigma$ level.

Note that if the clustering of the red and blue galaxies were identical, the larger average distance for the red galaxies compared to the blue galaxies (see Fig. 15) would yield lower A_W for the red galaxies than for the blue galaxies. The opposite effect is observed. Moreover, if the larger number of red galaxies (in the first 4 magnitude intervals

in Fig. 20) in the red sample (8986) compared to the blue sample (7259, see Table 10) is caused by large random errors at the limit of the catalogues, as seen in section 5.3.2, these would tend to dilute the A_W for the red sample. The detected increased clustering strength for the red sample over the blue sample is therefore a lower limit on the amplitude difference with colour. The apparent flattening of A_W with I_{median} for red galaxies in Fig. 20 may be due to the incompleteness of red objects at faint magnitudes as discussed above.

The difference in clustering amplitudes which we measure for our red and blue samples agrees with observations by Neuschaefer et al. (1995), Lidman & Peterson (1996) and Roche et al. (1996). Neuschaefer et al. find that disk-dominated galaxies (blue $V - I$) have marginally lower A_W than bulge-dominated galaxies (red $V - I$) using HST multi-colour fields. Similarly, Roche et al. observe a 3σ difference in A_W for a sample divided into objects bluer or redder than $b - r = 1.64$. Lidman & Peterson see a weak difference between two samples separated by $V - I = 1.5$. Other authors don't see any difference between blue and red-selected samples, such as Woods and Fahlman (1997) for a separation of $V - I = 1.3$, Brainerd et al. (1995) for $(g - r) = 0.3$, Le Fèvre et al. (1996) in the spatial correlation length of the CFRS for rest-frame $(U - R)_{AB} = 1.38$, and Infante & Pritchet (1995) for $(J - F) = 1$. In all these cases excepting Infante & Pritchet, who used photographic plates, both the number of galaxies and the angular scale of the surveys are small. It might be possible that in these surveys cosmic variance hides a weak signal.

7. Discussion

7.1. Limber's formula

Limber's formula (written here as eq. [15] and [16]) relating $\omega(\theta)$ and $\xi(r)$ is strongly dependent on the shape of the redshift distribution $N(z)$ which depends on the characteristic absolute magnitude M^* and slope α of the luminosity functions of the different types of galaxies (eq. [18]). Locally, these parameters cover a wide range of values with regard to the environment and the morphological types of the galaxies (Binggeli et al., 1988; Lin et al., 1999; Marzke et al., 1998; Bromley et al., 1998; Galaz and de Lapparent, 2000). No reasons lead us to think that galaxies would show less diversity at higher redshifts. Recent observations (in UV, IR, X, and γ) of space-borne observatories do provide evidence in this direction as well as the discordant measurements of the LF by the CFRS and CNOC2. Hence, a prior knowledge of the detailed luminosity functions is necessary to go beyond a phenomenological description of the clustering of galaxies.

Our computed r_0 is credible only if the correct luminosity functions have been used in Limber's formula: this would guarantee that the modeled $N(z)$ is close to the true redshift number distributions for each galaxy type.

Segregating galaxies into red and blue samples based on observed colour, as we do here, is also a crude first step, and should rather be performed using intrinsic colour or, even better, spectral type (cf section 6.3). These in turn would require knowledge of the galaxy redshifts. Approximate redshifts can also be obtained along with spectral type for multi-band photometric surveys using photometric redshift techniques (Koo, 1999). Because none of the required functions and distributions are available for our UH8K sample, we emphasize that the reported results can only be taken as phenomenological, and all the comments on the deduced clustering must be taken with caution.

7.2. The cosmological parameters

Most authors take for granted that different cosmological parameters only lead to minor differences in the evolution of clustering, compared to the effects due to the uncertain luminosity function. Figure 16, to 20 do show that for a given luminosity function different cosmological parameters induce different values of r_0 and ϵ . From our models, r_0 differs by more than 15% between the Λ flat and Open universes. These differences cannot yet be distinguished with the present data (up to $z \sim 1$). The dispersion between the different observations (Fig. 21) precludes any derivation of the cosmological parameters.

Given a CFRS luminosity function, the Λ flat universe gives the better fits to galaxy number counts, and clustering evolution of our sample ($\epsilon = 0 - 0.8$). This is in agreement with a current (though controversial) interpretation of recent type Ia supernovae results (Schmidt et al., 1998; Perlmutter et al., 1999). Notwithstanding the numerous modern methods to measure the cosmological parameters, the present analysis shows that future surveys containing 10^6 galaxies with known luminosity functions per galaxy type and redshift interval to $z \sim 1$ will be required to provide good constraints on cosmological parameters using this technique.

7.3. The evolution of clustering

Figure 21 shows the decrease of the amplitude of the angular correlation of our sample compared to most of the other recent measurements made in the I band (Brainerd and Smail, 1998; Campos et al., 1995; Woods and Fahlman, 1997; Postman et al., 1998; Lidman and Peterson, 1996; Neuschaefer and Windhorst, 1995; McCracken et al., 2000b). We applied a magnitude translation between Neuschaefer & Windhorst i magnitude and our I magnitude of $I = i - 0.7$.

In the magnitude range $I=20-22$, our results are in good agreement with most of these results except those of Campos et al, which have the highest amplitude, and on the low side, those of Lidman & Peterson and of McCracken et al., 3 times lower in amplitude. Postman et

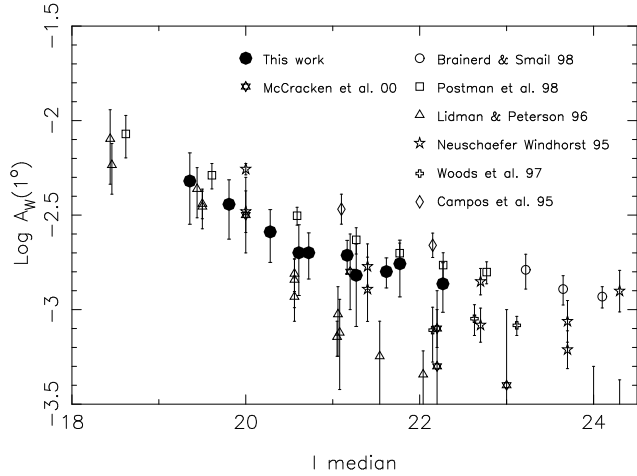


Fig. 21. Same as Fig. 16. Our measurements are compared with recent measurements found in the literature.

al., Woods et al., and Neuschaefer & Windhorst obtain intermediate values at $I_{median} > 22$.

Postman et al. observe a flattening of A_W for scales $> 1'$ and $I > 21$. The measurements of Brainerd & Smail extend the flattening of A_W observed by Postman et al. to $I \sim 24$. We also find a possible flattening in the decrease of A_W beyond $I \sim 21$. The most probable explanation for such high dispersion of about a factor ten between the different measurements of A_W is the dependence of A_W on the square of the number density. Cosmic variance may account for most of the discrepancies. The rest may be attributable to systematic errors of the estimators due to different spatial or magnitude samplings.

As pointed out by Neuschaefer & Windhorst (1995), a flattening of the slope δ (see eq. [14]) with the redshift or with apparent magnitude would lower the theoretical curve for A_W derived with Limber's formula (eq. [16]). Hence, smaller A_W would still be compatible with a small ϵ , or a high Ω_0 . In other words, clustering would grow faster at smaller scales than at larger scales. The flattening of the spatial correlation function is predicted by N-body simulations (Davis 1985; Kauffmann 1999a; 1999b). Neuschaefer & Windhorst parameterize the flattening of the slope $\gamma(z)$ with redshift z as: $\gamma(z) = 1.75(1+z)^{-C}$, where $C \simeq 0.2 \pm 0.2$. Postman et al. (1998) derive $C = 0.35 \pm 0.10$ with a slightly different parameterization: $\gamma(z) = 1.8(1+z)^{-C}$.

8. Conclusions

In this paper, we present measurements of the angular correlation function for a sample of $\sim 20,000$ galaxies to $I < 22.5$, and $V < 23.5$ observed with the CFHT UH8K mosaic CCD camera over a contiguous area of $\sim 30' \times 90'$. The main conclusions are the following:

- The amplitude of the angular correlation function of the complete sample decreases monotonically through the entire range of magnitude intervals.

- The flattening in the decrease of the amplitude, observed by Postman et al., is marginally confirmed by our analysis.

- The best model to fit the evolution of the amplitude of our sample is the combination of the CFRS luminosity function with mild luminosity evolution of late-type galaxies and no evolution of early-type galaxies, a Λ flat universe, a clustering evolution with $\epsilon > 0$, and a comoving correlation length of $r_0 \simeq 3.7 \pm 0.5 h^{-1}$ Mpc at $z \sim 0.50$. This is in agreement with the local measurements of r_0 with the clustering evolution predicted by CDM hierarchical clustering models.

- Red-selected galaxies show higher amplitudes of correlation than blue selected galaxies.

The deep multi-band photometric surveys which are in preparation should determine whether these observational results on the evolution of clustering are due to an inadequate definition of the luminosity functions of the different types of galaxies or whether the actual clustering differences reflect different formation histories of disk-dominated vs bulge-dominated galaxies. Ideally, one would like to measure the spatial two-point correlation function for each galaxy type, and for different redshift intervals. The luminosity functions and their evolution with redshift must be measured accordingly in order to closely model the observed redshift distribution of the sources. Application of photometric redshift techniques (Arnouts, 2000 priv. comm.) to the deep extension of the EIS survey (da Costa & Renzini, 1999) (<http://www.eso.org/science/eis>) should provide new constraints on these functions. Another deep survey which will also allow to address these issues is the LZT survey (Hickson et al., 1998), which will provide accurate redshifts to $\sigma_z \simeq 0.05$ and reliable spectral types for $\sim 10^6$ galaxies to $z \sim 1$. This will allow a more detailed study of the evolution of A_W . Note that the measured evolution of the clustering amplitude with redshift in these surveys might also provide useful constraints on the cosmological parameters.

Acknowledgements. The authors would like to thank Jean-Pierre Picat who kindly accepted to do the UH8K observations, Jean-Charles Cuillandre for the UH8K data calibration service, Stéphane Colombi for sharing his expertise on the error analysis and for his count-in-cells routines, B. Roukema for providing his catalogue prior to publication, S. Arnouts for many discussions, and Gary Mamon for his careful reading of the manuscript. R.A.C. thanks the Fonds FCAR for a post-doctoral fellowship.

References

- Arnouts, S., D'Odorico, S., Cristiani, S., Zaggia, S., Fontana, A., and Giallongo, E., 1999, *A&A* 341, 641
Bahcall, J. N., 1986, *ARA&A* 24, 577

- Baugh, C. M., Benson, A. J., Cole, S., Frenk, C. S., and Lacey, C. G., 1999, *MNRAS* 305, L21
- Bernstein, G. M., 1994, *ApJ* 424, 569
- Bertin, E. and Arnouts, S., 1996, *A&A* 117, 393
- Bingeli, B., Sandage, A., and Tammann, G. A., 1988, *ARA&A* 26, 509
- Brainerd, T. G., Law, C. J., Brauher, J., Djorgovski, S. G., and Banas, K., 1999, *astro-ph/9908148*
- Brainerd, T. G. and Smail, I., 1998, *ApJ* 494, L137
- Brainerd, T. G., Smail, I., and Mould, J., 1995, *MNRAS* 275, 781
- Bromley, B. C., Press, W. H., Lin, H., and Kirshner, R. P., 1998, *ApJ* 505, 25
- Bruzual, G. A. and Charlot, S., 1993, *ApJ* 405, 538
- Burstein, D. and Heiles, C., 1982, *AJ* 87, 1165
- Campos, A., Yepes, G., Carlson, M., Klypin, A. A., Moles, M., and Joergensen, H., 1995, in *Clustering in the Universe*, S. Maurogordato, C. Balowski, C. Tao, & J. Trân Thanh Vân (eds), p. 403
- Carlberg, R., Yee, H., Morris, S., Lin, H., Hall, P., Patton, D., Sawicki, M., and Shepherd, C., 2000, to be published in *ApJ*, *astro-ph/9910250*
- Carlberg, R. G. and Charlot, S., 1992, *ApJ* 397, 5
- Cole, S., Ellis, R. S., Broadhurst, T. J., and Colless, M. M., 1994, *MNRAS* 267, 541
- Cole, S., Treyer, M. A., and Silk, J., 1992, *ApJ* 385, 9
- Connolly, A. J., Szalay, A. S., and Brunner, R. J., 1998, *ApJ* 499, L125
- Couch, W. J., Jurcevic, J. S., and Boyle, B. J., 1993, *MNRAS* 260, 241
- Cowie, L. L., Lilly, S. J., Gardner, J., and McLean, I. S., 1988, *ApJ* 332, L29
- Cuillandre, J. C., 1996, Ph.D. thesis, Université Paul Sabatier, Physics
- Cuillandre, J. C., 1998a, in private comm., <http://www.cfht.hawaii.edu/~jcc/Flips/flips.html>
- Cuillandre, J. C., 1998b, in private comm., <http://www.cfht.hawaii.edu/~jcc/Detectors/UH8K/uh8kcal.html>
- da Costa, L., and Renzini, A., 1999, *Looking Deep in the Southern Sky*, Proc. ESO/Australia Workshop, Sydney, eds. R. Morganti, W. Couch, Springer-Verlag, p. 34
- Davis, M., Efstathiou, G., Frenk, C. S., and White, S. D. M., 1985, *ApJ* 292, 371
- Davis, M. and Faber, S. M., 1998, in *Wide Field Surveys in Cosmology*, 14th IAP meeting, eds S. Colombi, Y. Mellier, & B. Raban, Paris: Editions Frontières, p. 333.
- de Lapparent, V., Geller, M. J., and Huchra, J. P., 1988, *ApJ* 332, 44
- Dressler, A., 1980, *ApJ* 236, 351
- Driver, S. P., Phillipps, S., Davies, J. I., Morgan, I., and Disney, M. J., 1994, *MNRAS* 266, 155
- Efstathiou, G., Bernstein, G., Tyson, J. A., Katz, N., and Guhathakurta, P., 1991, *ApJ* 380, L47
- Ferguson, H. C. and Babul, A., 1998, *MNRAS* 296, 585
- Fioc, M. and Rocca-Volmerange, B., 1997, *A&A* 326, 950
- Galaz, G. and de Lapparent, V., 1998, in *Wide Field Surveys in Cosmology*, 14th IAP meeting, eds S. Colombi, Y. Mellier, & B. Raban, Paris: Editions Frontières, p. 157
- Galaz, G. and de Lapparent, V., 2000, in prep.
- Gardner, J. P., Sharples, R. M., Carrasco, B. E., and Frenk, C. S., 1996, *MNRAS* 282, L1
- Gaztañaga, E., 1994, *MNRAS* 268, 913
- Geller, M. J., Kurtz, M. J., and de Lapparent, V., 1984, *ApJ* 287, L55
- Groth, E. J. and Peebles, P. J. E., 1977, *ApJ* 217, 385
- Guzzo, L., Bartlett, J. G., Cappi, A., Maurogordato, S., Zucca, E., Zamorani, G., Balkowski, C., Blanchard, A., Cayatte, V., Chincarini, G., Collins, C., Maccagni, D., Macgillivray, H., Merighi, R., Mignoli, M., Proust, D., Ramella, M., Scaramella, R., Stirpe, G. M., and Vettolani, G., 1998, in *Wide Field Surveys in Cosmology*, 14th IAP meeting, eds S. Colombi, Y. Mellier, & B. Raban, Paris: Editions Frontières., p. 85
- Hauser, M. G. and Peebles, P. J. E., 1973, *ApJ* 185, 757
- Hickson, P., Borra, E. F., Cabanac, R., Chapman, S. C., de Lapparent, V., Mulrooney, M., and Walker, G. A., 1998, *Proc. of SPIE* 3352, 226
- Hudon, J. D. and Lilly, S. J., 1996, *ApJ* 469, 519
- Infante, L. and Pritchet, C. J., 1995, *ApJ* 439, 565
- Kauffmann, G., Colberg, J. M., Diaferio, A., and White, S. D. M., 1999, *MNRAS* 307, 529
- Koo, D. C. and Szalay, A. S., 1984, *ApJ* 282, 390
- Koo, D. C., 1999, *ASP Conf. Series*, 191, eds. R. Weymann, L. Storrie-Lombardi, M. Sawicki, R. Brunner, p. 3
- Landolt, A. U., 1992, *AJ* 104, 340
- Landy, S. D. and Szalay, A. S., 1993, *ApJ* 412, 64
- Le Fevre, O., Hudon, D., Lilly, S. J., Crampton, D., Hammer, F., and Tresse, L., 1996, *ApJ* 461, 534
- Le Fevre, O., Vettolani, G., Maccagni, D., Mancini, D., Picat, J. P., Mellier, Y., Mazure, A., Arnaboldi, M., Charlot, S., Cuby, J. G., Guzzo, L., Scaramella, R., Tresse, L., and Zamorani, G., 1998, in *Wide Field Surveys in Cosmology*, 14th IAP meeting, eds S. Colombi, Y. Mellier, & B. Raban, Paris: Editions Frontières., p. 327
- Lidman, C. E. and Peterson, B. A., 1996, *MNRAS* 279, 1357
- Lilly, S. J., Le Fevre, O., Crampton, D., Hammer, F., and Tresse, L., 1995, *ApJ* 455, 50
- Lilly, S. J., Le Fevre, O., Hammer, F., and Crampton, D., 1996, *ApJ* 460, L1
- Limber, D. N., 1953, *ApJ* 117, 134
- Limber, D. N., 1954, *ApJ* 119, 655
- Lin, H., Yee, H. K. C., Carlberg, R. G., Morris, S. L., Sawicki, M., Patton, D. R., Wirth, G., and Shepherd, C. W., 1999, *ApJ* 518, 533
- Loveday, J., Efstathiou, G., Peterson, B. A., and Maddox, S. J., 1992, *ApJ* 400, L43

- Loveday, J., Maddox, S. J., Efstathiou, G., and Peterson, B. A., 1992, *ApJ* 442, 457
- Maddox, S. J., Efstathiou, G., Sutherland, W. J., and Loveday, J., 1990a, *MNRAS* 243, 692
- Maddox, S. J., Efstathiou, G., Sutherland, W. J., and Loveday, J., 1990b, *MNRAS* 242, 43P
- Mamon, G. A., 1998, in *Wide Field Surveys in Cosmology, 14th IAP meeting*, eds S. Colombi, Y. Mellier, & B. Raban, Paris: Editions Frontières, p. 323.
- Marzke, R. O., da Costa, L. N., Pellegrini, P. S., Willmer, C. N. A., and Geller, M. J., 1998, *ApJ* 503, 617
- McCracken, H. J., Metcalfe, N., Shanks, T., Campos, A., Gardner, J. P., and Fong, R., 2000a, *MNRAS*, 311, 707
- McCracken, H. J., Shanks, T., Metcalfe, N., Fong, R., and Campos, A., 2000b, to be published in *MNRAS*
- Metzger, M. R., Luppino, G. A., and Miyazaki, S., 1995, in *AAS Meeting*, 187, 7305
- Monet, D. G., 1998, in *AAS Meeting*, 193, 12003
- Neuschaefer, L. W., Griffiths, R. E., Im, M., Ratnatunga, K. U., Wyckoff, E., Windhorst, R. A., Gordon, J. M., Pascarelle, S. M., Schmidtke, P. C., Ellis, R. S., Glazebrook, K., Shanks, T., Elson, R. A. W., Gilmore, G., Schade, D. J., Green, R. F., Huchra, J. P., Illingworth, G. D., Koo, D. C., Forbes, D., Schmidt, M., and Tyson, A., 1992, in *American Astronomical Society Meeting*, Vol. 181, p. 4502
- Neuschaefer, L. W., Ratnatunga, K. U., Griffiths, R. E., Casertano, S., and Im, M., 1995, *ApJ* 453, 559
- Neuschaefer, L. W. and Windhorst, R. A., 1995, *ApJ* 439, 14
- Peebles, P., 1980, *The large-scale structure of the universe*, Princeton University Press, Princeton N.J., p. 435
- Peebles, P. J. E. and Hauser, M. G., 1974, *ApJS* 28, 19
- Perlmutter, S., Aldering, G., Goldhaber, G., Knop, R. A., Nugent, P., Castro, P. G., Deustua, S., Fabbro, S., Goobar, A., Groom, D. E., Hook, I. M., Kim, A. G., Kim, M. Y., Lee, J. C., Nunes, N. J., Pain, R., Pennypacker, C. R., Quimby, R., Lidman, C., Ellis, R. S., Irwin, M., McMahon, R. G., Ruiz-Lapuente, P., Walton, N., Schaefer, B., Boyle, B. J., Filippenko, A. V., Matheson, T., Fruchter, A. S., Panagia, N., Newberg, H. J. M., Couch, W. J., and The Supernova Cosmology Project, 1999, *ApJ* 517, 565
- Phillipps, S., Fong, R., Fall, R. S. E. S. M., and Macgillivray, H. T., 1978, *MNRAS* 182, 673
- Postman, M., Lauer, T. R., Szapudi, I., and Oegerle, W., 1998, *ApJ* 506, 33
- Ratcliffe, A., Shanks, T., Parker, Q. A., and Fong, R., 1998, *MNRAS* 296, 173
- Roche, N. and Eales, S. A., 1999, *MNRAS* 307, 703
- Roche, N., Shanks, T., Metcalfe, N., and Fong, R., 1993, *MNRAS* 263, 360
- Roche, N., Shanks, T., Metcalfe, N., and Fong, R., 1996, *MNRAS* 280, 397
- Roukema, B. F. and Peterson, B. A., 1994, *A&A* 285, 361
- Schechter, P., 1976, *ApJ* 203, 297
- Schmidt, B. P., Suntzeff, N. B., Phillips, M. M., Schommer, R. A., Clocchiatti, A., Kirshner, R. P., Garnavich, P., Challis, P., Leibundgut, B., Spyromilio, J., Riess, A. G., Filippenko, A. V., Hamuy, M., Smith, R. C., Hogan, C., Stubbs, C., Diercks, A., Reiss, D., Gilliland, R., Tonry, J., Maza, J., Dressler, A., Walsh, J., and Ciardullo, R., 1998, *ApJ* 507, 46
- Tucker, D. L., Oemler, A., J., Kirshner, R. P., Lin, H., Shectman, S. A., Landy, S. D., Schechter, P. L., Muller, V., Gottlober, S., and Einasto, J., 1997, *MNRAS* 285, L5
- Villumsen, J. V., Freudling, W., and da Costa, L. N., 1997, *ApJ* 481, 578
- Woods, D. and Fahlman, G. G., 1997, *ApJ* 490, 11
- Yee, H. K. C., Ellingson, E., and Carlberg, R. G., 1996, *ApJS* 102, 269
- Yoshii, Y., 1993, *ApJ* 403, 552